# Seismic Attenuation Structure of the Seattle Basin, Washington State, from Explosive-Source Refraction data

by Qin Li, William S.D. Wilcock, Thomas L. Pratt, Catherine M. Snelson, and Thomas M. Brocher

**Abstract.** We used waveform data from the 1999 SHIPS (Seismic Hazard Investigation of Puget Sound) seismic refraction experiment to constrain the attenuation structure of the Seattle basin, Washington State. We inverted the spectral amplitudes of compressional- and shear-wave arrivals for source spectra, site responses, and one- and two-dimensional $Q^{-1}$ models at frequencies between 1 and 40 Hz for *P*-waves and 1 and 10 Hz for *S*-waves. We also obtained $Q^{-1}$ models from $t^*$ values calculated from the spectral slopes of *P*-waves between 10 and 40 Hz. One-dimensional inversions show that $Q_p$ at the surface is 22 at 1 Hz, 130 at 5 Hz and 390 at 20 Hz. The corresponding values at 18 km depth are 100, 440 and 1900. $Q_s$ at the surface is 16 and 160 at 1 Hz and 8 Hz, respectively, increasing to 80 and 500 at 18 km depth. The $t^*$ inversion yields a $Q_P$ model that is consistent with the amplitude inversions at 20 and 30 Hz. The basin geometry is clearly resolved in the $t^*$ inversion, but the amplitude inversions only imaged the basin structure after removing anomalously high amplitude shots near Seattle. When these shots are removed, we infer that $Q^{-1}$ values may be ~30% higher in the center of the basin than the one-dimensional models predict. We infer that seismic attenuation in the Seattle basin will significantly reduce ground motions at frequencies at and above 1 Hz, partially countering amplification effects within the basin.

# Introduction

Western Washington State has a significant earthquake hazard from three distinct earthquake sources. The Cascadia subduction zone megathrust surfaces about 50-100 km off the coast of the Pacific Northwest and hosts great (magnitude ~9) earthquakes every 600 years on average (Atwater, 1996; Goldfinger et al., 2003). The subducted Juan de Fuca ocean plate produces Benioff zone earthquakes at a depth of ~60 km below Puget Sound, including the 1949 magnitude 7.1 Olympia earthquake, the 1965 magnitude 6.5 Seattle earthquake and the 2001 magnitude 6.8 Nisqually earthquake (Frankel et al., 2002). The shallow crust is also prone to infrequent large earthquakes; at least one magnitude ≥7 earthquake occurred on the Seattle and Tacoma faults ~1100 years ago (Bucknam et al., 1992; Nelson et al., 2003; Sherrod et al., 2004).

The Puget Sound region is underlain by thick sequences of Cenozoic sedimentary rocks that are deformed by west- and northwest-trending faults and folds (Johnson et al., 1994; 1996; Pratt et al., 1997) resulting from margin-parallel shortening (Wells et al., 1998) and north directed thrusting (Pratt et al., 1997). The north-directed thrusting has produced three thick Cenozoic sedimentary basins, the Everett, Seattle and Tacoma basins, separated by regions of uplifted and folded Tertiary sedimentary strata and Eocene volcanic bedrock. These basins are important for hazard analyses because they appear to focus and trap seismic energy, leading to strong site amplification effects during large earthquakes (e.g., Graves et al., 1998; Frankel et al., 2002; Pratt et al., 2003). The Seattle basin is of particular concern because it is the largest of these basins with a maximum thickness of about 9 km and underlies the largest concentration of population and infrastructure in the state.

There are two complementary approaches to estimating the site amplification effects of the Seattle basin. The first is to compare the amplitudes of recent earthquakes recorded inside and

outside the basin (Frankel et al., 1999; Hartzell et al., 2000; Pratt et al., 2003). The second is to develop numerical models of seismic propagation through the basin for large earthquakes (Frankel and Stephenson, 2000). The latter approach requires knowledge of the seismic structure of the region. Recent seismic work provides constraints on the velocity structure of the basin from tomographic studies (Brocher et al., 2001; Snelson, 2001; Crosson et al., 2002; Van Wagoner et al., 2002; Snelson et al., 2005). In contrast, there are no measurements of attenuation within the basin even though high attenuation in the basin sediments will act to counteract the effects of focusing, particularly at higher frequencies (e.g., Olsen et al., 2003; Pratt et al., 2003; Pratt and Brocher, 2005).

Current attenuation models for the Pacific Northwest were obtained by applying regression techniques to records from Western Canada Telemetered Network stations around Vancouver Island (Atkinson, 1995). A Brune source model (Brune, 1970) and a geometric spreading of $r^{-1}$ were assumed. The anelastic attenuation coefficient for *S*-waves given by these regressions is $Q_s = 380f^{0.39}$ for all earthquakes, and a somewhat lower $Q_s = 174f^{0.58}$, for crustal earthquakes only. Since the regressions were for bedrock sites, they likely underestimate the attenuation in the Seattle basin and other sedimentary basins.

In this paper, we estimate the *P*- and *S*-wave attenuation structure in the Seattle basin using waveforms from explosive-source data from an east-trending refraction profile across the Seattle Basin (Brocher et al., 2000). Using seismic velocity models obtained from the same data set (Snelson, 2001; Snelson et al., 2005), we apply two different spectral techniques to obtain one- and two-dimensional attenuation models along the profile.

## Attenuation Tomography Methods

The attenuation of a plane seismic wave can be expressed as:

$$A(t) = A_0 e^{-\pi f t/Q} \quad , \tag{1}$$

where $A(t)$ is its amplitude at time $t$, $A_0$ is its amplitude at time zero, $f$ is the frequency, and $Q$ is a quality factor that is defined as:

$$\frac{1}{Q} = \frac{-\Delta E}{2\pi E}, \tag{2}$$

with $-\Delta E/E$ the fractional loss of energy per cycle of oscillation. For non-planar waves, equation (1) still holds provided the amplitudes are first corrected for the effects of geometrical spreading. In seismic attenuation studies, equation (1) is commonly written in an alternative form:

$$A(t) = A_0 e^{-\pi f t^*} \quad , \tag{3}$$

where $t^*$ is a measure of the cumulative seismic attenuation and is defined as an integral of the reciprocals of velocity, $V$ and $Q$ along the ray path, $s$:

$$t^* = \int_s \frac{1}{Q(s,f)V(s)} \, ds \quad . \tag{4}$$

A variety of methods are used to estimate the seismic attenuation of body waves in both the time and frequency domains (Tonn, 1989) but the most common methods estimate $t^*$ directly from spectral slopes (e.g., Bonilla et al., 1997; Wilcock et al., 1995) or differential $t^*$ ($\delta t^*$) from spectral ratios of $P$ to $P$-waves or $P$ to $S$-waves (e.g., Roth et al., 1999; Zucca and Evans, 1992).

In the frequency domain, the amplitude spectrum $X_{ij}(f)$ of a short window that encloses the phase of interest from the seismic record for the $i^{th}$ source and the $j^{th}$ receiver, can be described by the product:

$$X_{ij}(f) = S_i(f) P_{ij}(f) R_j(f) I_j(f) \quad , \tag{5}$$

where $S$ is the source spectrum; $P$ is the path effect, $R$ is the site response; and $I$ is the instrument response. The site response includes local effects occurring near a receiver, which are generally assumed independent of the source azimuth and incidence angle. The path effects include geometric spreading, short-leg multiples, multipathing, transmission losses at interfaces, phase conversions, intrinsic attenuation and scattering attenuation but are commonly approximated as the product of two terms:

$$P_{ij}(f) = G_{ij} \exp(-\pi f t^*_{ij}) \quad . \tag{6}$$

where $G_{ij}$ is a geometric spreading term which is assumed to be frequency independent, and $t^*_{ij}$ is defined as in equation (4) and can account for both intrinsic and scattering attenuation.

**Spectral Slope Inversion Method**

The spectral slope method requires that the amplitude spectrum defined in equation (5) first be corrected for the source spectrum, site response and instrument response to yield an estimate of the path effect. If we assume that $t^*$ is frequency independent, then taking the derivative of equation (6) with respect to frequency yields:

$$t^*_{ij} = -\frac{1}{\pi} \frac{d \ln(P_{ij})}{df} \quad . \tag{7}$$

The quantity $t^*$ can then be estimated from the slope of the logarithm of the corrected spectrum once the instrument response, source spectrum and site response are known.

To formulate the inverse problem to obtain a $Q^{-1}$ model from a set of $t^*$ measurements, we first write equation (4) in a discretized form:

$$t^*_{ij} = \sum_{k=1}^{N} V(x_k)^{-1} Q(x_k)^{-1} \delta S_k \quad , \tag{8}$$

where $N$ is the number of ray path segments and $x_k$ and $\delta S_k$ are the center point and length of the $k^{th}$ segment, respectively. If the velocity model and ray path are known, and a $Q^{-1}$ model is parameterized on grid of nodes with linear interpolation in between, equation (8) can then be written as:

$$t_{ij}^{*} = \sum_{l=1}^{M} a_l \cdot Q_l^{-1}, \qquad (9)$$

where $M$ is total number of nodes and $a_l$ is a weight factor calculated for the $l^{th}$ mode in the $Q^{-1}$ model. When compiled for a set of source-receiver pairs, equation (9) forms a linear equation set that can be written as:

$$\mathbf{t^*} = \mathbf{A_q q} \ , \qquad (10)$$

where $\mathbf{t^*}$ is a vector of $t^*$ values**,** $\mathbf{A}_q$ is a sparse matrix of nodal weights for the $Q^{-1}$ model and $\mathbf{q}$ is a vector of $Q^{-1}$ model values.

**Corrected Spectral Amplitude Inversion Method**

An important advantage of the spectral slope method is that it requires no correction for geometric spreading but it does have two significant disadvantages. First, it requires knowledge of the site responses and source spectra, neither of which are well known *a priori* for many experiments. Second, it is dependent on the assumption of frequency-independent Q. In tectonically active areas several studies suggest $Q$ is strongly frequency dependent, particularly below 10 Hz (Adams and Abercrombie, 1998; Kinoshita, 1994; Yoshimoto et al., 1998). The first limitation can be overcome at least in part by fitting a source model (Lees and Lindley, 1994) or taking spectral ratios (Roth et al., 1999; Zucca and Evans, 1992) but to take into account the frequency dependence of the quality factor $Q^{-1}$, we developed a second method that corrects amplitude spectra for instrument response and geometric spreading, and we formulate an inverse

problem to obtain source spectra, site responses and $Q^{-1}$ at each frequency of interest. We then use source spectra and site responses to obtain $t^*$ estimates for spectral slopes by correcting amplitude spectra in equation (5) in order to obtain the path effect of equation (6). This leads directly to estimates of $t^*$ using equation (7) which are used for the inverse problem of equation (10).

Using equations (5) and (6), a corrected amplitude spectrum can be written as:

$$X'_{ij}(f) = \frac{X_{ij}(f)}{I_j(f) \cdot G_{ij}} = S_i(f) \cdot R_j(f) \cdot \exp\left(-\pi f t^*_{ij}(f)\right). \qquad (11)$$

where $t^*_{ij}$ is now frequency dependent. Taking logarithms yields:

$$\ln\left(X'_{ij}(f)\right) = \ln\left(S_i(f)\right) + \ln\left(R_j(f)\right) - \pi f t^*_{ij}(f) \ . \qquad (12)$$

Using the steps outlined in equations (8) and (9) to discretize the last term leads to a linear set of equations at each frequency which can be written

$$\mathbf{x} = \begin{bmatrix} \mathbf{A}_q & \mathbf{A}_s & \mathbf{A}_r \end{bmatrix} \begin{bmatrix} \mathbf{q} \\ \mathbf{s} \\ \mathbf{r} \end{bmatrix} \ , \qquad (13)$$

where $\mathbf{x}$ is a vector of the logarithms of corrected spectral amplitudes; $\mathbf{A}_s$ and $\mathbf{q}$ are as defined for equation 10; $\mathbf{A}_s$ and $\mathbf{A}_r$ are matrices used to identify sources and receivers for each record; and $\mathbf{s}$ and $\mathbf{r}$ are vectors of the source spectra and site responses, respectively.

There are strong tradeoffs between the different terms in equation (13) and particularly between the near surface $Q^{-1}$ and site response. Although the equation can be solved in a single step with appropriate regularization, we found that a two-step iterative solution was the simplest means to ensure a stable inversion that minimized variations in the $Q^{-1}$ model. Our approach was first to calculate the source spectra and site responses assuming a reasonable $Q^{-1}$ model, and second, to calculate a $Q^{-1}$ model based on the source spectrum and site response from the first

step. This process was repeated iteratively until the solution converged. In practice we found that the method converged quickly and the results were insensitive to the initial $Q^{-1}$ model. At each frequency of interest we solved successively for the best fitting spatially invariant, one-dimensional, and two dimensional $Q^{-1}$ models using the final results from previous inversion as the starting point for the next. The source spectra and site responses derived from one- and two-dimensional inversions are very similar.

Another problem with equations (10) and (13) is that they do not include the physical constraint that $Q$ must be positive. Such constraints can be added to a least squares solution (Lawson and Hanson, 1974), but the method is not computationally efficient when the number of parameters is large. Instead we chose to parameterize the attenuation in term of the perturbation to $\ln(Q^{-1})$ rather than $Q^{-1}$ (Wilcock et al., 1995). We can rewrite equation (10) and the attenuation portion of equation (13) in a general form:

$$\begin{aligned} \mathbf{b} &= \mathbf{A}_q\mathbf{q} = \mathbf{A}_q(\mathbf{q}_0 + \delta\mathbf{q}) \approx \mathbf{A}_q[\mathbf{q}_0 + \mathbf{q}_0\delta\ln(\mathbf{q})] \\ \mathbf{b} - \mathbf{A}_q\mathbf{q}_0 &\approx \mathbf{A}_q\mathbf{q}_0\delta\ln(\mathbf{q}) = \mathbf{A}_q{}'\delta\ln(\mathbf{q}) \end{aligned}, \qquad (14)$$

where **b** is either **t*** in equation (10) or **x** in equation (13) corrected for source and site effects, $\mathbf{q}_0$ is an initial $Q^{-1}$ model, $\delta\mathbf{q}$ is the perturbation to initial model, and $\mathbf{A}_q$' is a matrix with each element given by:

$$A'_{q\,ij} = q_j A_{q\,ij} \ , \qquad (15)$$

Equation (15) is linear for $\delta\ln\mathbf{q}$ but not for **q,** so the solution for **q** has to be obtained iteratively. For each iteration step, $\delta\ln\mathbf{q}$ is calculated and used to update the $Q^{-1}$ model and the process is repeated until the solution converges. In practice the method is very stable, the solutions converge within a few iterations, and they are insensitive to the initial $Q^{-1}$ model.

For our data set we solved for the source spectra and site responses in equation (13) using a least squares method (e.g., Menke, 1989), without adding additional constraints but obtaining a stable solution to equation (15) required additional regularization. Our approach was to minimize a combination of the data misfit, the roughness of $\delta\ln\mathbf{q}$, and the magnitude of $\delta\ln\mathbf{q}$. The data misfit is given by:

$$\chi^2 = (\mathbf{x'} - \mathbf{A}_q \cdot \mathbf{q}_0 - \mathbf{A'}_q \, \delta \ln \mathbf{q})^T \mathbf{C}^{-1} (\mathbf{x'} - \mathbf{A}_q \cdot \mathbf{q}_0 - \mathbf{A'}_q \, \delta \ln \mathbf{q}) \qquad (16)$$

where **C** is a the data variance and can be written as:

$$C_{ij} = \delta_{ij} \sigma_i^2 \text{ (no sum)} \qquad (17)$$

where $\delta_{ij}$ is an identity matrix, and $\sigma_i$ is an estimate of the uncertainty of the $i^{\text{th}}$ observation. For equation (10) $\sigma^2$ can be obtained from the variance of the least squares straight line fit to the corrected spectrum, while for equation (13) relative values of $\sigma^2$ are estimated from the reciprocal of the signal to noise ratio (SNR). A smoothing constraint, which minimizes the roughness of the $\delta\ln\mathbf{q}$ model is given by:

$$R_f{}^2 = (\mathbf{L} \cdot \delta \ln \mathbf{q})^T (\mathbf{L} \cdot \delta \ln \mathbf{q}) \qquad (18)$$

where **L** is a two-dimensional second-order roughness operator. The magnitude of $\delta\ln\mathbf{q}$ is given by:

$$D_v{}^2 = (\delta \ln \mathbf{q})^T (\delta \ln \mathbf{q}) \qquad (19)$$

Combining these terms yields:

$$\gamma^2 = \chi^2 + \alpha^2 R_f{}^2 + \alpha^2 \beta^2 D_v{}^2 \qquad (20)$$

where $\alpha$ and $\beta$ are smoothing coefficients which control the trade-offs among misfit, model size, and smoothness. A solution for $\delta\ln\mathbf{q}$ that minimizes $\gamma^2$ is obtained by a least squares solution to:

$$\begin{bmatrix} \mathbf{C}^{-1/2}\mathbf{A}'_q \\ \alpha\mathbf{L} \\ a\beta\mathbf{I} \end{bmatrix} d\ln(\mathbf{q}) = \begin{bmatrix} \mathbf{C}^{-1/2}(\mathbf{b} - \mathbf{A}_q\mathbf{q}_0) \\ \mathbf{0} \\ \mathbf{0} \end{bmatrix} \tag{21}$$

The value of **q** is then updated and the method repeated until the solution converges.

## Field Data

We apply these methods to waveform data acquired over the Seattle basin during the 1999 Seismic Hazard Investigation in Puget Sound (SHIPS) experiment, known as "1999 SHIPS" or "Dry SHIPS". This experiment acquired a 116-km-long east-west oriented seismic refraction profile across the Seattle basin (Fig. 1) using a total of 38 explosive shots ranging in size from 11 kg (25 lbs) to 1270 kg (2800 lbs). These sources were detonated at ~4 km intervals along the profile and were recorded by 1000 land seismometers, of which 897 were deployed along the profile at a nominal spacing of 100 m. Two types of geophones were used: 324 seismometers were Mark Products L4A type geophone sensors with 2 Hz resonant frequency, while the rest utilized Mark Products L-28 type geophone sensors with 4.5 Hz resonant frequency. Most of the seismometers comprised a single vertical geophone but 231 seismometers had three orthogonal 4.5 Hz, L-28 type geophones.

The data quality for the *P*-waves is generally high. The seven largest shots with sizes ≥910 kg (2000 lbs) yielded clear arrivals over most of the profile (Fig 2a-b) and useful signal to noise from 1 Hz to ≥30 Hz. Most of the smaller shots generated identifiable arrivals up to ranges of 40 km. The only region of low signal to noise is near Seattle ($X$ = 55-71 km in the model coordinates of Fig. 1) where the background noise levels are high (Fig 2a). With the exception of shot 6 at the western end of the profile (Fig. 1), the only sources providing useful signal to

noise ratios near Seattle are smaller shots located nearby such as shots 25 and 31. The data quality for *S*-waves on the horizontal channels of the 231 three-component seismometers is lower than the *P*-wave data (Fig. 2c). Explosions are unreliable sources of *S*-wave energy and this energy is generally attenuated more efficiently than for *P*-waves. As a result *S*-waves having useful signal to noise ratios are limited to a subset of shots and to frequencies below 10 Hz.

Although the SHIPS experiment was not specifically designed with attenuation studies in mind, it is the only seismic refraction data set in the region with such a high density of receivers, and it thus provides a unique opportunity to study attenuation properties of the Seattle basin.

## Data Processing

### Spectrum Estimation

We estimated spectra from the waveform data using a multiple-taper method with $2\pi$ prolate tapers (Park et al., 1987). This method provides an optimal spectrum estimate for a time window by minimizing spectral leakage and the variance of the estimate. As the length of the time window increases, the variance of the estimate averaged over a finite bandwidth decreases, but longer spectral estimation windows may include unwanted and scattered phases. After inverting data using various spectral estimation window lengths, we found that a 1-s-long window yielded the most consistent inversion results. However, $2\pi$ prolate tapers applied to 1-s long windows produce spectral estimates that are averaged over a bandwidth of 4 Hz. At frequencies below the resonant frequency of the geophone the instrument response drops off rapidly and the spectral estimate is dominated by frequencies at the upper end of the estimation

bandwidth. For this reason we used 4-s-long windows for estimating spectra at 1 Hz, 1-s- and 4-s-long windows at 2 Hz, and 1-s-long windows at higher frequencies.

Examples of seismograms and their corrected spectra are shown in Figure 3. The signal spectra were obtained from windows aligned with the phase onset and the noise spectra were obtained from a time window immediately before the onset of the first arrival. We excluded records at ranges <5 km because the signal windows at these ranges are often contaminated by strong surface waves and secondary refracted arrivals. To minimize interference from scattered *P*-wave energy, the *S*-wave spectra were obtained from the SH phase by rotating the two horizontal records into a direction perpendicular to the profile. All spectra were corrected for the instrument response. The *P*-wave records have the best SNR between 5 and 10 Hz, and the signal-to-noise ration (SNR) decreases steadily at higher frequencies (Fig. 3).

For P-wave amplitude inversions we excluded all estimates having a SNR below 2, and we examined frequencies from 1 to 40 Hz. Our P-wave amplitude data set comprised ~4700 records at 2 Hz, ~5300 records at 10 Hz, and ~2300 records at 30 Hz (Table 1). For the *S*-waves the SNR was much lower and we limited the data to frequencies between 1 and 10 Hz. The S-wave amplitude data set comprised ~630 and ~350 records at 2 Hz and 8 Hz, respectively (Table 1).

To estimate $t^*$ from spectral slopes, we corrected the spectra for instrument response and for the frequency-dependent source spectra and site responses obtained from amplitude inversions. We used a least squares method to fit straight lines to the slopes of the logarithm of the corrected spectral amplitudes between 10 Hz and the smaller of 40 Hz and the highest frequency at which the signal to noise is greater than 2 (Fig. 3b). The resulting data set comprises ~4500 $t^*$ values (Table 1).

**Ray Tracing and Geometric Spreading**

The amplitude inversions require correction for geometric spreading. We calculated geometrical spreading from two-dimensional *P*-wave and *S*-wave velocity models (Fig. 4) derived from travel time data from 1999 SHIPS experiment (Snelson, 2001; Snelson et al., 2005). The Vidale (1988) algorithm, used for the velocity inversion, is computationally efficient and accurately calculates first arrival wave paths and travel times for triplications and shadow zones. However, when we attempted to use this method to calculate geometric spreading corrections within the Seattle basin, we found that the results were often unstable at ranges greater than ~60 km: the geometric spreading corrections changed rapidly with range and were inconsistent with the data.

To avoid this problem we implemented a point and shoot ray tracing method. The Eikonal equation can be split into two first-order ordinary differential equations:

$$\begin{cases} \dfrac{d\mathbf{k}}{dt} = (\mathbf{k} \bullet \nabla c) \cdot \mathbf{k} - \nabla c \\ \mathbf{k} = \dfrac{d\mathbf{x}}{ds} = \dfrac{d\mathbf{x}}{dt} \cdot \dfrac{dt}{ds} = \dfrac{1}{c} \cdot \dfrac{d\mathbf{x}}{dt} \end{cases}, \qquad (22)$$

where **k** is a unit vector that points in the direction of wave propagation; **x** is the position which specifies ray paths; *s* is arc distance along the ray path; and *c* is seismic velocity. Given the initial position and incidence angle, the pay path can be traced by solving these two vector equations. We used the Runge-Kutta method (Press et al., 1992) to obtain numerical solutions to these ordinary differential equations.

Ray paths calculated for the unsmoothed velocity models (Fig. 5a) include both triplications and shadow zones for which ray theory predicts infinite and zero amplitudes, respectively. To eliminate these undesired features, we smoothed the velocity model with a cubic spline smoothing algorithm (De Boor, 1978). The recalculated ray paths shown in Figure 5b were used to make two corrections. First, we divided each amplitude by the cosine of the

incidence angle to account for non-vertical incidence. Second we obtained a geometric spreading correction by measuring the surface area of the wavefront subtended by a bundle of rays within a small range of incidence angles (Lay and Wallace, 1995). Figure 6 compares examples of geometric spreading for both *P*-waves and *S*-waves with the predictions for a simple $r^{-a}$ amplitude decay model where r is the range and a is a constant between 1 and 2. The ray-theoretical geometric spreading predictions are similar for both *P*-wave and *S*-waves and relatively uniform across the basin. A $r^{-1.6}$ decay model yields the best fit to these predictions. Figure 7a shows the form of the predicted *P*-wave geometric spreading for shot 6 and various $r^{-a}$ models overlying the amplitude data at 10 Hz. The ratios of the geometric spreading and amplitude data are the input for the amplitude inversions.

## Results

### Corrected Spectral Amplitude Inversions

Using the inversion method outlined above, we inverted *P*-wave amplitudes at frequencies between 1 and 40 Hz and *S*-wave amplitudes between 1 and 10 Hz for source spectra, site responses and spatially invariant, one- and two-dimensional $Q^{-1}$ models. For the *P*-waves, source spectral amplitudes are generally highest between 5 and 10 Hz, and decrease progressively at higher frequencies (Fig. 8a). For the *S*-waves, source spectral amplitudes are almost flat from 1 to 8 Hz (Fig. 8b). The most prominent feature in the site responses is a peak (i.e., high amplitudes) near the center of the basin, and a tendency toward increasing peak amplitudes with frequency (Fig. 9). Although our site responses are similar to the site responses used in ground motion studies (Frankel et al., 1999; Pratt et al., 2003), the two are not directly

comparable because ours are not normalized to bedrock stations but are instead adjusted so that the mean logarithm of the response for all stations at each frequency is unity.

An example of 10 Hz *P*-wave spectral amplitudes after correction for geometric spreading, source spectrum, and site response is provided in Figure 7b. The spectral amplitudes are scattered and the root mean squared residual of the base-10 logarithm of the amplitudes is 0.56 relative to the best fitting two-dimensional model.

The $Q^{-1}$ models obtained from the inversions are sensitive to the values of the smoothing coefficients $\alpha$ and $\beta$ in equation 20. Figure 10 shows the results of a one-dimensional inversion for $Q_P^{-1}$ at 5 Hz for a range of $\alpha$ and a fixed $\beta$ of 0.15. For $\alpha > 100$, $Q_P$ has a nearly uniform value of 230. As $\alpha$ decreases below 100 the models show a progressively larger increase in $Q_P$ with depth. For $\alpha \leq 10$, the $Q_P$ model is quite rough. In the absence of reliable estimates of data uncertainty, the choice of smoothing coefficient is necessarily subjective. We base our choice on inspecting the smoothness of the models (Fig. 10a) and the curvature of the tradeoff between data misfit and model smoothness (Fig. 10b). For this set of inversions our preferred value of $\alpha$ is 40.

Figure 11 shows our preferred one-dimensional *P*- and *S*-wave *Q* models for the Seattle basin at various frequencies and Table 1 summarizes the inversion parameters and misfits. These one-dimensional inversions provide a large variance reduction relative to the best fitting spatially invariant Q models (Table 1). At all frequencies *Q* increases substantially with depth. The *P*-wave results (Fig. 11a) show that $Q_P$ is strongly frequency dependent below 20 Hz. For example, $Q_P$ at the surface increases from 22 at 1 Hz to 130 at 5 Hz and 390 at 20 Hz. The corresponding values at the base of the model at 18 km depth are 100, 440 and 1900. $Q_S$ values are always lower than the corresponding $Q_P$ values and are also strongly frequency dependent over the

range of frequencies analyzed (Fig 11b). Between 1 and 8 Hz $Q_S$ increases from 16 to 160 at the surface and from 80 to 500 at 18 km depth.

Two-dimensional inversions of the full set of *P*-wave amplitudes for $Q^{-1}$ are shown in Figures 12a-f. The results at 1 Hz and 2 Hz in Figures 12a-b are derived from 4-s-long time windows while Figures 12c-f are for 1-s-long windows. The two-dimensional inversions yield only a small variance reduction relative to the preferred one-dimensional models (Table 1) even for models that are quite rough. The misfits resulting from the one-dimensional inversions (e.g., Figure 7b) are dominated by scatter rather than systematic trends. We prefer two-dimensional solutions with relatively high levels of smoothing that minimize model roughness at horizontal scales below 10 km.

Despite the small variance reduction, the solutions show evidence for a basin structure with higher $Q_P^{-1}$ in the center of the model at greater depths. This is particularly apparent at 5 and 10 Hz (Figures 12d-e), the frequencies with the most amplitude data (Table 1) and the most uniform ray coverage (Figure 13a). However, at shallower depth the models are characterized by a region of low attenuation near the center of the model in the Seattle metropolitan area. This feature is particularly pronounced at 2 and 20 Hz (Figures 11c and 11e). This region of low near-surface $Q$ coincides with the region of high site response amplitudes (Figure 9). In this region the SNR is poor as evidenced by the lower ray-path density (Figure 13b), and the amplitude data are limited to a few shots at relatively small ranges and shot 6 at the west end of the line. At the time of the experiment it was noted that some shots within the Seattle area caused anomalously high amplitudes at shorter ranges, possibly because of energy being trapped in the shallow sediments (Brocher et al., 2000). To understand this bias, we repeated the 10 Hz inversion after excluding these anomalous shots (Fig. 12g). The shallow structure near Seattle is then

constrained only by data from shot 6 and the smoothing constraints. The results show a better defined basin structure, with $Q_P^{-1}$ near the center of the model ~30% higher than in the one-dimensional model.

The number of amplitude data for the *S*-waves is much lower (Table 1) and we only show results at 4 Hz (Fig. 14) because the spatial variations in the other inversions are very similar. The 4-Hz model has a relatively flat structure although there is a small decrease in shallow $Q_S^{-1}$ near the center of the model. The ray density in this region is very low (Fig. 13c) and is only based on nearby shots, so we cannot be sure whether this feature is real or is an artifact of these anomalous shots at shorter ranges.

**Spectral Slope Inversion**

Our preferred one- and two-dimensional *P*-wave attenuation models obtained from inverting $t^*$ values are shown in Figure 11a and 12h, respectively and the inversion parameters and misfits are summarized in Table 1. These inversions represent an average of the attenuation structure between 10 and 40 Hz. The one-dimensional model (Fig. 11a) is remarkably similar to those obtained from amplitude inversions at 20 and 30 Hz: $Q$ is about 300 at surface of the basin and 2200 at 18 km depth. The two-dimensional model (Fig. 12h) shows a basin-shaped structure despite a decrease in ray density near the center of the profile (Fig. 13d). The surface $Q_P^{-1}$ increases from 0.0015 and 0.0025 at the western and eastern ends of the profile respectively to values in excess of 0.0045 near the center. After allowing for the frequency dependence of $Q_P$ (Fig. 11a), these results are reasonably consistent with the results of the two-dimensional inversion at 10 Hz that excludes anomalous shots in the Seattle metropolitan region (Fig. 12g), although the surface gradients in $Q_P^{-1}$ are much higher in the $t^*$ inversion.

## Discussion

We applied two different spectral inversion techniques to data from an east-trending refraction profile to image the attenuation structure within the Seattle basin. The study has a number of limitations, including the use of data not designed for attenuation studies, the use of short time windows, and the reliance on a velocity model. The data also show significant scatter. In this section we first address these limitations and then proceed to show that despite these caveats the results are self-consistent, and consistent with other studies. We conclude by discussing the implications for ground motions in the Seattle basin.

One limitation of this study is that the data acquisition was not designed with attenuation measurements in mind. The majority of the instruments used 4.5 Hz geophones with limited response at lower frequencies, and as a result the number of amplitude observations with useful signal to noise ratios decreases substantially below 5 Hz. The number of *S*-wave observations is much lower than for *P*-waves because less than a quarter of the seismometers included three component geophones and all of these used 4.5 Hz sensors.

A second limitation is that the methods rely on the assumption that the spectrum of a short time window is representative of the total attenuation (intrinsic and scattering) of the phase of interest and is not corrupted by the presence of other arrivals. For most of the inversions, we used a 1-s-long window and we excluded shots at ranges less than 5 km because the windows were often corrupted by surface waves and secondary refracted waves. However, at 1 Hz and for some of the 2-Hz inversions, we used a 4-s-long window to achieve the necessary spectral resolution. This longer time estimation window increases the probability that the spectral estimates are biased by other phases. Propagation effects such as short-leg multiples,

multipathing, head waves, transmission losses at interfaces and phase conversions may bias the attenuation measurements and these biases are hard to quantify.

A third limitation is that our inversions are strongly dependent on the velocity models for the Seattle basin (Snelson, 2001; Snelson et al., 2005). The models are used to calculate ray paths for all the inversions and to calculate geometric spreading corrections for the amplitude inversions. Errors in the geometric spreading correction are difficult to quantify and will affect the absolute values of Q and its frequency dependence. At the lowest frequencies considered (1 Hz), the seismic wavelength is several kilometers; a significant fraction of the ~6 km basin depth beneath the 1999 SHIPS profile and thus, the ray-theoretical and shortest-time paths used in the inversions may not be fully representative of the Fresnel zone sampled by the phase of interest. At higher frequencies, the geometric spreading corrections are likely to be significantly in error. To stabilize the geometric spreading calculations we smoothed the velocity models, and thus the fine scale velocity structure that focuses or defocuses rays is not included in our corrections.

It is clear from the amplitude and $t^*$ data (Fig. 3c-d) that individual measurements have a great deal of scatter. For the $t^*$ data, this scatter presumably results from the relatively small bandwidth of the measurements coupled with the sensitivity of a least squares straight line fit to exterior points (Menke, 1989). Wilcock (1992) found that the scatter of $t^*$ estimates obtained from marine explosion source data decreased substantially when the estimation bandwidth increased from 10 to 30 Hz to 10 to 60 Hz. Although some of our t* estimates were obtained between 10 and 40 Hz, the majority were limited to a maximum frequency of <30 Hz (e.g., Fig. 3) because of poor signal to noise at higher frequencies.

To understand the scatter in the amplitude data, we calculated the root mean square (RMS) difference in the logarithmic amplitude measurements as a function of receiver spacing. The

results (Fig. 15) show that the corrections for the site response and geometric spreading reduce the RMS scatter by about 40%. The plots for the corrected data extrapolate to an RMS scatter for coincident receivers (i.e., $\Delta X = 0$) between 0.1 and 0.2. This scatter is equivalent to amplitude variations of ~25% to 60% for seismometers spaced <0.5 km apart. It is larger than the estimated instrument calibration error of 15-20% at these frequencies, but probably not unreasonable for field data given the practical difficulties of coupling and leveling many geophones in the field. The scatter of both the uncorrected and corrected data increases substantially with receiver spacing out to ~5 km and then remains relatively constant. This suggests that much of the scatter in the amplitude data may result from focusing and defocusing by fine scale layering and lateral velocity heterogeneities at scales of up to a few kilometers. Further support for this idea comes from the fact that the RMS scatter is larger at higher frequencies where one would expect higher sensitivity to fine scale structure. For example at 20 Hz the RMS scatter of the corrected data is >0.3 (Fig. 15b) compared with ~0.25 at 5 Hz (Fig. 15a).

Despite scatter in the data, the inversions yield results that are consistent both internally and with other studies. In the one-dimensional models $Q$ increases progressively with depth and the amplitude inversions show that Q is strongly frequency dependent below ~20 Hz with $Q$ increasing with frequency. The $P$-wave models obtained from amplitude data at 20 and 30 Hz are remarkably similar to the model obtained from t* measurements between 10 and up to 40 Hz (Fig. 11a).

Figure 16 compares frequency-dependent regional $Q_S$ models (Atkinson, 1995) with the results of our one-dimensional amplitude inversions at two depths; a depth of 4 km that lies near the middle of the Seattle basin and a depth of 14 km that lies well below its base. The regional

models significantly underpredict the attenuation within the basin sedimentary rocks, but below the basin our results agree quite closely with those of the regional model. At 5 Hz, for example, we measure $Q_S$ of 150 and 350 at 4 km and 14 km depths, while the regional model predicts 442 (Atkinson, 1995).

Our results are reasonably compatible with those from other sedimentary basins. For example, Olsen *et al.* (2003) use a three-dimensional numerical simulation to estimate $Q_S$ in the Los Angeles Basin at frequencies of ≤0.5 Hz. They infer that $Q_S$ may be as low as ~10 in surficial sediments that have *S*-wave velocities of ~0.5 km/s. We do not measure $Q_S$ below 1 Hz and our surface value at this frequency is 15. The difference could be explained by frequency dependence but it may also be indicative of the low resolution of our models near the surface. Since we excluded spectra from ranges of < 5 km, our inversions include no rays that turn at depths of less than ~0.4 km. Thus, a shallow low velocity layer with very low $Q$ cannot be resolved by the inversions, and the attenuation caused by the shallow layer would be largely accounted for by a constant offset to the source spectra.

A striking feature of our *P*-wave amplitude inversions is the strong frequency dependence of $Q_P$ below ~20 Hz (Fig. 11) and the relatively weak frequency dependence at higher frequencies, particularly at greater depths (Fig. 16). At the depth of 14 km, the best-fit power law relationship of frequency dependence is $Q_p = 77 f^{1.01}$ and $Q_p = 1040 f^{0.16}$ for frequencies between 1 and 20 Hz and 20 and 40 Hz, respectively (Fig. 16). At the depth of 4 km, the relationship is $Q_p = 44 f^{0.81}$ over frequencies between 1 and 40 Hz. The *S*-wave results were obtained over a smaller frequency band but also show a strong frequency dependence. At 4 km depth the best fitting power laws are $Q_p = 63 f^{1.10}$ at 1-5 Hz and $Q_p = 164 f^{0.64}$ at 5-10 Hz, while

at 14 km depth a relationship $Q_p = 29 f^{0.99}$ fits the results at all frequencies. It is possible that some of the observed frequency dependence is due to errors in the geometric spreading correction; corrections that over predict the amplitudes at large ranges would lead to a power law coefficient of unity. However such errors cannot account for the change in the power law coefficient observed at shallower depths for both *P*- and *S*-waves

Other studies report similar frequency dependence in tectonically active areas. For example, in a study of data from the Cajon Pass borehole in southern California, Adams and Abercrombie (1998) find that the total *S*-wave *Q* is strongly frequency dependent below 10 Hz ($\propto f^{1.8}$) but only weakly so at higher frequencies ($\propto f^{0.34}$). In southern Kanto area of central Japan, Kinoshita (1994) measure $Q_S$ at frequencies between 0.5 and 16 Hz and found that $Q_S$ increases as $f^{0.7}$ above 0.8 Hz. At frequencies between 25 and 102 Hz, Yoshimoto et al. (1998) find that $Q_S$ is only weakly frequency dependent ($\propto f^{0.12}$) in the western Nagano Prefecture of Japan although they report a much stronger frequency dependence for $Q_P$ ($\propto f^{0.66}$).

The ratio $Q_p/Q_s$ varies between 1.0 and 1.6 in the frequency range of 1 to 10 Hz, and averages 1.2. These values are much lower than the ratio of 2.25 expected for a Poisson's solid if the attenuation is dominated by intrinsic attenuation in shear (Anderson, 1967). These values imply, not surprisingly, that Q is significantly influenced by scattering. Our value of $Q_p/Q_s$ lies within the range reported for other studies. For example, in the Cajon Pass $Q_p/Q_s$ increases from 1.4 to 2.0 from the surface towards the bottom of the Cajon borehole (Abercrombie, 1997). In Japan Yoshimoto et al. (1998) find $Q_s/Q_p < 1$ for all frequencies between 25 and 102 Hz.

Our two-dimensional inversions yield only a small variance reduction relative to one-dimensional inversions (Table 1). Nevertheless, the $t^*$ inversion (Fig. 12h) shows a basin structure at all depths. The *P*-wave amplitude inversions at 5 and 10 Hz (Figs. 12d-e), the

frequencies with the most data, also resolve the basin geometry at greater depths. However, near the surface the amplitude inversions at all frequencies are characterized by low values of Q (Figs. 12c, 12f) and high site responses (Fig. 9) in the Seattle metropolitan area. As we explained above, this is probably an artifact of the high noise levels in the Seattle metropolitan area coupled with the anomalously high amplitudes of some nearby shots. When shots in the Seattle metropolitan area excluded, the results at 10 Hz show a clear basin (Figs. 12g). An important implication of the two-dimensional inversions is that $Q^{-1}$ may be up to 30% lower than the true $Q^{-1}$, between 2 and 20 Hz. This difference could also account for the difference between the surface $Q_S$ of 16 at 1 Hz in the one-dimensional inversion and the value of ~10 reported by Olsen *et al.* (2003) for the Los Angeles Basin.

To model how much attenuation in the Seattle basin reduces ground motions, we calculated the total change in amplitude for a plane wave propagating vertically from 10 km depth to the surface using our one-dimensional Q models (Fig. 17). At higher frequencies, the *S*-wave calculations assumed $Q_P/Q_S$ = 1.2. For *P*-waves the amplitudes are reduced ~20% at 1 Hz and more then 30% at 30 Hz; for *S*-waves, basin attenuation decreases amplitudes ~35% at 1 Hz and over 50% at 30 Hz. As noted above, these amplitude decreases may be underestimated by ~30% and they will also be larger for scattered arrivals, reverberations and phases that propagate horizontally such as surface waves. Pratt *et al.* (2003) noted that the amplitudes of seismic waves above about 7 Hz from local earthquakes and blasts are smaller in the basin than at bedrock sites, which suggests significant attenuation counters the amplification effects of decreased impedance in the shallow sediments. Pratt and Brocher (2005) analyzed S-wave arrivals in the 2 to 20 Hz frequency range from local earthquakes, and concluded that Qs values in the sedimentary basins beneath the Puget Lowland range from 5-40 near the surface to ~250 in the deep basin sediments

(7 km depth). These results are in broad agreement with ours. We conclude that attenuation within the Seattle basin will significantly reduce ground motions, at least partly countering amplification effects within the basin.

## Conclusions

We developed and implemented an algorithm to invert amplitude spectra from controlled source data for 1-D and 2-D attenuation structure. We applied this algorithm to data recorded by the 1999 SHIPS experiment in the Seattle basin, to examine the attenuation within the basin. The 1999 SHIPS experiment was not designed for attenuation studies, yet it provided a unique dataset with which to study the attenuation structure of the Seattle basin. We developed Q estimates using both t* and spectral amplitudes for frequencies between 1 and 40 Hz. Despite the large scatter in individual amplitude and $t^*$ measurements, our study yielded consistent results between methods. $Q$ increases with depth and with frequency up to 20 Hz, and the attenuation levels within the Seattle Basin are about 5 to 2 times higher than regional levels from 1Hz to 10 Hz. At 1 Hz we infer minimum $Q_S$ and $Q_P$ of 15 and 22, respectively. In the middle of the basin, the frequency dependence of the $Q_P$ can be fit by power laws of $f^{0.2}$; beneath the basin, the frequency dependence decreases above 20 Hz, and the corresponding power laws are $f^{0.2}$ for 1-20 Hz and $f^{0.2}$ for 20-40 Hz, respectively. The low Q values within the Seattle basin determined by our study are consistent with previous observations of de-amplification of weak ground motions for frequencies greater than 7 Hz (Pratt et al., 2003; Pratt and Brocher, 2005).

## Acknowledgement

We thank all those who participated in planning and carrying out the 1999 SHIPS experiment. This work was partially supported by the U.S Geological Survey Cooperative Agreement 01-HQ-AG-001, the U.S. Geological Survey Earthquake Hazard Reduction Program and the U.S. Geological Survey Urban Hazards Initiative. Instruments were provided by the PASSCAL program of the Incorporated Institutes for Seismology (IRIS) and by the Geological Survey of Canada. The manuscript has benefited from review by Art Frankel, Donna Eberhart-Phillips and two anonymous reviewers.

Department of Earth and Space Science, Box 351310
University of Washington
Seattle, WA 98195-1310
(Q.L.)

School of Oceanography, Box 357940
University of Washington
Seattle WA 98195-7940
(W.S.D.W.)

Department of Geoscience
University of Nevada
Las Vegas NV 89154-4010
(C.M.S.)

U.S. Geological Survey
School of Oceanography, Box 357940
University of Washington
Seattle, Washington 98195
(T.L.P.)

U.S. Geological Survey
345 Middlefield Road, MS 977
Menlo Park, California 94025
(T.M.B.)

# Figure Captions

**Figure 1**. Map of the east-west oriented 1999 SHIPS refraction profile across Puget Sound (areas of land shaded) showing the 897 receivers (black triangles) and explosion locations (grey circles) along the main refraction line. Numbers label shots referenced in the text or figures. Outline of the Seattle basin (grey solid line) and location of the Seattle fault (grey dashed line) are shown based on the interpretation of a Bouguer gravity anomaly map (Finn *et al*., 1991) and seismic reflection data (Pratt, 1997). The scale bar shows the $X$ coordinates used for this study; $X$ = 0 km corresponds to the western end of the line.

**Figure 2**. (a) Record section showing *P*-wave arrivals for shot 10, located near the eastern end of the line ($X$ = 117.5 km; Fig. 1). The plot shows every $10^{th}$ trace along the entire profile. Bold horizontal lines show the arrival time picks, and asterisks indicate that the trace was used in the 10 Hz attenuation inversions. The vertical axis is reduced travel time corrected at 6.5 km/s. The traces have been band-pass filtered between 2 and 40 Hz. (b) As for (a) except all traces are shown at ranges of 96-114 km near the western end of the profile. (c) As for (a) except showing *SH*-wave arrivals for shot 6, located near the western end of the profile (X = 7.1 km; Fig. 1), for all 3-component stations at ranges of 74-90 km. The reduction velocity is 3.5 km/s. Note that some traces are very noisy (e.g., those at ranges of 77.5 km and 80 km) but that all the traces in this record section have acceptable signal to noise at 2-4 Hz.

**Figure 3**. Five examples of *P*-wave seismograms, amplitude spectra, and t* estimates for shot 6 at ranges varying from 113 km (a) to 5 km (e). The left hand plots show the seismogram labeled with the range. Vertical lines show time windows used to obtain amplitude spectra for the *P*-wave (solid lines) and for a noise sample (dashed lines). The right hand plots show the corresponding *P*-wave (solid line) and noise (dot-dashed line) amplitude spectra calculated using multi-taper spectral analysis and corrected for instrument response, source spectrum and site response. The estimates of $t^*$ (labeled) were obtained according to equation (7) with a least squares straight line fit (dashed line) over the frequency band shown by the vertical solid lines.

**Figure 4**. (a) *P*-wave and (b) *S*-wave velocity models derived from the 1999 SHIPS data (Snelson, 2001; Snelson et al., 2005). The models are parameterized on 1 km x 1 km grids. The bold line shows the base of the Seattle Basin as delineated by the $V_P$ = 4.5 km/s contour. (c) Smoothed versions of the *P*-wave and (d) *S*-wave velocity models used to calculate the geometric spreading calculation (see text).

**Figure 5**. Ray paths calculated by the point and shoot method for (a) the unsmoothed *P*-wave model (Fig. 4a) and (b) the smoothed version of this model (Fig 4c). The MATLAB function *csaps* that reproduces the Fortran routine SMOOTH of De Boor (1978) was used with a smoothing parameter of 0.1. Smoothing eliminates triplications and shadow zones and stabilizes geometric spreading calculations. The bold line shows

the base of the Seattle Basin as delineated by the $V_P$ = 4.5 km/s contour (Snelson, 2001; Snelson et al., 2005).

**Figure 6**. Geometric spreading calculated by the point and shoot method (solid lines) for smoothed (a) *P*-wave and (b) *S*-wave velocity models for shots 6 and 10 at opposite ends of the profile (Fig. 1). In (a) we show geometric spreading calculated for shot 6 with the unsmoothed *P*-wave velocity model (dashed line). Note the unrealistic spike in amplitudes near $X$ = 80 km. Other unsmoothed models, not shown, predict regions of zero and infinite amplitudes. Dotted lines show various $r^{-a}$ decay models where $r$ is the range and $a$ ranges from 1 to 2. The best fit to the geometric spreading calculations is obtained with $a \approx 1.6$.

**Figure 7.** (a) Uncorrected spectral amplitudes at 10 Hz for shot 6 (small dots) plotted against location on the profile. Curves show several $r^{-a}$ amplitude decay models (dashed lines) where $r$ is the range and $a$ varies from 1 to 2 and the geometric spreading calculated for shot 6 with the smoothed P-wave velocity model (solid line) (see text). (b) Spectral amplitudes at 10 Hz (small dots) corrected for ray divergence, source spectrum and site responses (see text) plotted against the location on the profile. Curves show the corrected amplitudes smoothed with a 10-km wide cosine taper (large dots that overlap to form a bold line), the predictions of the best fitting spatially invariant $Q$ model (dot-dashed line) and our preferred one-dimensional (solid line) and two-dimensional (dashed line) $Q$ models. (c) Spectral slope $t^*$

estimates and model predictions for shot 6 plotted against location on the profile using the same conventions as (b).

**Figure 8**. Source spectral amplitudes obtained from (a) *P*-wave and (b) *S*-wave amplitude inversions. The shot locations are shown in Figure 1 and size of the shots are as follows: shot 6, 1270 kg (2800lbs); shot 12, 23 kg (50 lb); shot 25, 180 kg (400 lbs); and shot 35, 57 kg (125 lbs). Note that the frequency limits differ between the two plots.

**Figure 9**. Site responses from one-dimensional amplitude inversions for (a) *P*-waves at frequencies of 1, 2, 5, 10, 20, and 30 Hz and (b) *S*-waves at frequencies of 1, 2, 4, and 8 Hz. Small dots show site responses obtained from the inversions and big dots which overlap to form interrupted bold lines show the same site responses smoothed with a 5-km-wide cosine taper. The results were obtained with 1-s-long data windows except at 1 Hz were a 4-s-long window was used.

**Figure 10**. Results of a one-dimensional inversion of *P*-wave amplitudes at 5 Hz illustrating the tradeoff between data misfit and model smoothness. (a) $Q$ models for various choices of the smoothing parameter $\alpha$. (b) Plot of the root mean square data misfit $\sqrt{\quad}$, where $N$ is the number of observations, versus the roughness constraints, (equations 16-20). All models shown have $\beta = 0.15$ and our preferred model for this set of inversions has $\alpha = 40$.

**Figure 11**. (a) Preferred one-dimensional $Q_p$ models derived from the amplitude inversions at 1, 2, 5, 10, 15, 20 and 30 Hz (solid lines) and from the *t** inversion (dashed line). (b) Preferred one-dimensional $Q_s$ models derived from the amplitude inversions at 1, 2, 4, and 8 Hz (solid lines). $Q_p$ models are also plotted for comparison (dashed lines). The 1 Hz results for both $Q_p$ and $Q_s$ are calculated from a 4-s data analysis window; the other inversions are for a 1-s-long window. The models are parameterized on a 2 km x 2 km grid. Horizontal lines at ~6 km depth indicated the approximate depth of the Seattle basin beneath Seattle.

**Figure 12**. Preferred two-dimensional $Q_p^{-1}$ models. (a-b) Models obtained at 1 and 2 Hz from an amplitude inversion for a 4-s-long window. (c-f) Models obtained at 2, 5, 10 and 20 Hz from an amplitude inversion for a 1-s-long window. (g) Model obtained at 10 Hz for an amplitude inversion that excludes anomalous shots near Seattle. (h) Model obtained from inversion of spectral slope t* values. All models are parameterized on a 4 km x 2 km grid. The bold line shows the base of the Seattle Basin as delineated by the $V_P$ = 4.5 km/s contour (Snelson, 2001; Snelson et al., 2005).

**Figure 13**. Shaded contour plot of the ray path hit count in blocks with horizontal and vertical dimensions of 4 km and 2 km, respectively, for the *P*-wave amplitude data at (a) 10 Hz and (b) 20 Hz; (c) the *S*-wave amplitude data at 4 Hz; and (d) the spectral slope *t** data.

**Figure 14**. Two-dimensional $Q_s^{-1}$ models obtained at 4 Hz from an amplitude inversion of a 1-s window. The bold line shows the base of the Seattle Basin as delineated by the $V_P$ = 4.5 km/s contour (Snelson, 2001; Snelson et al., 2005).

**Figure 15.** The root mean square (RMS) difference between the base-10 logarithms of pairs of amplitude measurements for the same shot as a function of the distance between the receivers, $\Delta X$. Differences for both uncorrected amplitudes (solid line) and amplitudes corrected for source spectrum and geometric spreading (dashed line) are shown at (a) 5 Hz and (b) 20 Hz. The RMS values are calculated for 0.5-km-wide $\Delta X$ bins.

**Figure 16**. Q versus frequency at 4 km and 14 km depth for the one-dimensional *P*-wave (dots) and *S*-wave (triangle) amplitude inversions. Dashed lines show regional attenuation models of Atkinson (1995). The upper dashed line shows model ($Q_S = 380f^{0.38}$) for all earthquakes and the lower dashed line shows model ($Q_S = 174f^{0.58}$) for only shallow crustal earthquakes. Labeled solid lines show power law fits to our data.

**Figure 17** Plot showing the ratio of the amplitude at the surface to the amplitude at 10 km depth ($A_0/A_{10}$) against frequency for vertical propagation through the one dimensional $Q_P$ (solid) and $Q_S$ (dashed) models of Figure 11. The predictions from the regional $Q_S$ model for crustal earthquakes (Atkinson, 1995) are also shown (dot-dashed).

## References


Abercrombie, R.E. (1997). Near-surface attenuation and site effects from comparison of surface and deep borehole recordings, *Bull. Seism. Soc. Am. 87* **3**, 731-744.

Adams, D.A., and R.E. Abercrombie (1998). Seismic attenuation above 10 Hz in Southern California from coda waves recorded in the Cajon Pass borehole, *J. Geophy. Res. 103* **10**, 24,257-24,270.

Anderson, D.L. (1967). The anelasticity of the mantle, *Geophys. J. R. Astron. Soc. 14*, 135-164.

Atkinson, G.M. (1995). Attenuation and source parameters of earthquakes in the Cascadia region, *Bull. Seism. Soc. Am. 85* **5**, 1327-1342.

Atwater, B.F. (1996). Coastal evidence for great earthquakes in western Washington, in *Assessing earthquake hazards and reducing risk in the Pacific Northwest; Volume 1*, pp. 77-90, U.S. Geol. Surv.

Bonilla, L.F., J.H. Steidl, G.T. Lindley, A.G. Tumarkin, and R.J. Archuleta (1997). Site amplification in the San Fernando Valley, California: variability of site-effect estimation using the S-wave, coda, and H/V methods, *Bull. Seism. Soc. Am. 87* **3**, 710-730.

Brocher, T.M., T.L. Pratt, K.C. Miller, A.M. Trehu, C.M. Snelson, C.S. Weaver, K.C. Creager, R.S. Crosson, U.S. ten Brink, M.G. Alvarez, S.H. Harder, and I. Asudeh (2000). Report for explosion and earthquake data acquired in the 1999 Seismic Hazards Investigation of Puget Sound (SHIPS), Washington, *U.S. Geological Survey Open-file Report 2000-318*, 85 pp., 2000. http://geopubs.wr.usgs.gov/open-file/of00-318/.

Brocher, T.M., T. Parsons, R.A. Blakely, N.I. Christensen, M.A. Fisher, R.E. Wells, and the SHIPS Working Group (2001). Upper crustal structure in Puget Lowland, Washington: Results from 1998 Seismic Hazards Investigation in Puget Sound, *J. Geophy. Res.* 106, 13,541-13,564.

Brune, J.N. (1970). Tectonic stress and the spectra of seismic shear waves from earthquakes, *J. Geophy. Res. 75* **26**, 4997-5009.

Bucknam, R.C., E. Hemphill-Haley, and E.B. Leopold (1992). Abrupt uplift within the past 1700 years at southern Puget Sound, Washington, *Science 258*, 1611-1614.

Crosson, R.S., N.P. Symons, K.C. Creager, L.A. Preston, W.T. Van, T.M. Brocher, and M.A. Fisher (2002). Three-dimensional structure of the Cascadia forearc region from SHIPS active experiment and earthquake observations; tomographic inversion provides a high-resolution view into the core of the Cascadia forearc complex, in *The Cascadia subduction zone and related subduction systems; seismic structure, intraslab earthquakes and processes, and earthquake hazards*, *U.S. Geological Survey Open-File Report* 02-328 and *Geological Survey of Canada Open File 4350*, p. 33-34. http://geopubs.wr.usgs.gov/open-file/of02-328/.

De Boor, C. (1978). Smoothing and Least-squares Approximation; SMOOTH, L2APPR, in *A practical guide to splines*, pp. 235-276, Springer-Verlag, Berlin, West Germany.

Frankel, A.D., D.L. Carver, E. Cranswick, M.E. Meremonte, T. Bice, and D.E. Overturf (1999). Site response for Seattle and source parameters of earthquakes in the Puget Sound region, *Bull. Seism. Soc. Am. 89* **2**, 468-483.

Frankel, A.D., and W.J. Stephenson (2000). Three-dimensional simulations of ground motions in the Seattle region for earthquakes in the Seattle fault zone, *Bull. Seism. Soc. Am. 90*, 1251-1267.

Frankel, A.D., D.L. Carver, and R.A. Williams (2002). Nonlinear and linear site response and basin effects in Seattle for the M 6.8 Nisqually, Washington earthquake, Seism. Soc. Am. Bull. 92, 2090-2109.

Goldfinger, C., C.H. Nelson, J.E. Johnson, and the Shipboard Scientific Party (2003). Holocene earthquake records from the Cascadia subduction zone and north San Andreas fault based on precise dating of offshore turbidites, *Annu. Rev. Earth Planet. Sci*. **31**, 555-577.

Graves, R.W., A. Pitarka, and P.G. Somerville (1998). Ground-motion amplification in the Santa Monica area; effects of shallow basin-edge structure, *Bull. Seism. Soc. Am. 88* **5**, 1224-1242.

Hartzell, S., D. Carver, E. Cranswick, and A.D. Frankel (2000). Variability of site response in Seattle, Washington, *Bull. Seism. Soc. Am. 90* **5**, 1237-1250.

Johnson, S.Y., C.J. Potter, and J.M. Armentrout (1994). Origin and evolution of the Seattle Fault and Seattle Basin, Washington, *Geology 22* **1**, 71-74.

Johnson, S.Y., C.J. Potter, J.M. Armentrout, J.J. Miller, C. Finn, and C.S. Weaver (1996). The southern Whidbey Island fault: an active structure in the Puget Lowland, Washington, *Geol. Soc. Am. Bull. 108* **3**, 334-354.

Kinoshita, S. (1994). Frequency-dependent attenuation of shear waves in the crust of the southern Kanto area, Japan, *Bull. Seism. Soc. Am. 84* **5**, 1387-1396.

Lawson, C.L., and R.J. Hanson (1974). Solving Least Squares Problems, pp. 340, Englewood Cliffs, New Jersey.

Lay, T., and T.C. Wallace (1995). Body Waves and Ray Theory, in *Modern Global Seismology*, Academic Press.

Lees, J.M., and G.T. Lindley (1994). Three-dimensional attenuation tomography at Loma Prieta: inversion of $t^*$ for $Q$, *J. Geophy. Res.*, *99* **B4**, 6843-6863.

Menke, W. (1989). *Geophysical Data Analysis: Discrete Inverse Theory*, 285 pp., Academic Press, San Diego, CA.

Nelson, A.R., S.Y. Johnson, H.M. Kelsey, R.E. Wells, B.L. Sherrod, S.K. Pezzopane, L.A. Bradley, and R.D. Koehler, III (2003). Late Holocene earthquakes on the Toe Jam Hill fault, Seattle fault zone, Bainbridge Island, Washington, *Geol. Soc. Am. Bull*. **115**, 1388-1403.

Olsen, K.B., S.M. Day, and C.R. Bradley (2003). Estimation of Q for Long-Period (>2 sec) Waves in the Los Angeles Basin, *Bull. Seism. Soc. Am. 93* **2**, 627-638.

Park, J., C.R. Lindberg, and F.L. Vernon, III (1987). Multitaper spectral analysis of high-frequency seismograms, *J. Geophy. Res. 92* **12**, 12,675-12,684.

Pratt, T.L., and T.M. Brocher (2005). Site response and attenuation in the Puget Lowland, Washington State, *Bull. Seism. Soc. Am.*, in press.

Pratt, T.L., S. Johnson, C. Potter, W. Stephenson, and C. Finn (1997). Seismic reflection images beneath Puget Sound, western Washington State: the Puget Lowland thrust sheet hypothesis, *J. Geophy. Res. 102* **B12**, 27469-27489.

Pratt, T.L., T. Brocher, C.S. Weaver, K.S. Weaver, A.M. Trehu, K.C. Creager, and R.S. Crosson (2003). Amplification of seismic waves by the Seattle basin, Washington State, *Bull. Seism. Soc. Am. 93* **2**, 533-545.

Press, W.H., S.A. Teukolsky, W.T. Vetterling, and B.P. Flannery (1992). Integration of Ordinary Differential Equations, in *Numerical Recipes in C The Art of Scientific Computing*, Cambridge University Press.

Roth, E.G., D.A. Wiens, L.M. Dorman, J. Hildebrand, and S.C. Webb (1999). Seismic attenuation tomography of the Tonga-Fiji region using phase pair methods, *J. Geophy. Res. 104* **3**, 4795-4809.

Sherrod, B.L., T.M. Brocher, C.S. Weaver, R.C. Bucknam, R.J. Blakely, H.M. Kelsey, A.R. Nelson, and R. Haugerud, 2004, Holocene fault scarps near Tacoma, Washington, *Geology* 32, 9-12.

Snelson, C.M. (2001). Investigating crustal structure in western Washington and in the Rocky Mountains: implications for seismic hazards and crustal growth, PhD thesis thesis, University of Texas, El Paso.

Snelson, C.M., K.C. Miller, T.M. Brocher, and T.L. Pratt (2005). Seismic Amplification Within the Seattle Basin, Washington State: Insights from SHIPS Seismic Tomography Experiments, *Bull. Seism. Soc. Am., in preparation*.

Tonn, R. (1989). Comparison of seven methods for the computation of Q, *Phys. Earth Plan. Int. 55* **3-4**, 259-268.

Van Wagoner, T.M., R.S. Crosson, K.C. Creager, G. Medema, L. Preston, N.P. Symons, and T.M. Brocher (2002). Crustal structure and relocated earthquakes in the Puget Lowland,

Washington, from high-resolution seismic tomography, *J. Geophy. Res. 107* **12**, ESE 22-1 - 22-23, 10.10129/2001JB000710.

Vidale, J. (1988). Finite-difference calculation of travel times, *Bull. Seism. Soc. Am. 78* **6**, 2062-2076.

Wilcock, W.S.D. (1992). The seismic attenuation structure of the East Pacific Rise, PhD thesis thesis, MIT/WHOI Joint Program, Cambridge, MA.

Wilcock, W.S.D., S.C. Solomon, G.M. Purdy, and D.R. Toomey (1995). Seismic attenuation structure of the East Pacific Rise near 9 degrees 30 minutes N, *J. Geophy. Res. 100* **B12**, 24147-24165.

Yoshimoto, K., H. Sato, Y. Iio, H. Ito, T. Ohminato, and M. Ohtake (1998). Frequency-dependent attenuation of high-frequency P and S waves in the Upper Crust in Western Nagano, Japan, *Pure Appl. Geop. 153* **2-4**, 489-502.

Zucca, J.J., and J.R. Evans (1992). Active high-resolution compressional wave attenuation tomography at Newberry Volcano, Central Cascade Range, *J. Geophy. Res. 97* **B7**, 11,047-11,055.

**Table 1.** Summary of inversion results.

| Inversion | | Number of observations | Spatially Invariant $Q$ models | | One-dimensional $Q$ models | | | | Two-dimensional $Q$ models | | | |
|---|---|---|---|---|---|---|---|---|---|---|---|---|
| | | | $Q$ | Misfit[1] | $\alpha$ | $\beta$ | Misfit[1] | Variance Reduction[2] | $\alpha$ | $\beta$ | Misfit[1] | Variance Reduction[2] |
| *P*-wave | 1 Hz | 4117 | 65 | 0.49 | 45 | 0.15 | 0.36 | 90% | 25 | 0.12 | 0.34 | 10% |
| | 1 Hz [3] | 2796 | 65 | 0.61 | 45 | 0.15 | 0.42 | 110% | 25 | 0.12 | 0.41 | 6% |
| | 2 Hz | 4646 | 120 | 0.46 | 45 | 0.15 | 0.35 | 80% | 25 | 0.12 | 0.33 | 10% |
| | 5 Hz | 5504 | 255 | 0.53 | 45 | 0.15 | 0.41 | 60% | 25 | 0.12 | 0.39 | 11% |
| | 10 Hz | 5316 | 475 | 0.59 | 45 | 0.15 | 0.41 | 110% | 25 | 0.12 | 0.39 | 8% |
| | 10 Hz[4] | 4138 | 475 | - | 45 | 0.15 | 0.42 | - | 25 | 0.12 | 0.40 | 11% |
| | 20 Hz | 3782 | 915 | 0.68 | 45 | 0.15 | 0.45 | 130% | 25 | 0.12 | 0.43 | 11% |
| | 30 Hz | 2299 | 950 | 0.69 | 45 | 0.15 | 0.46 | 130% | 25 | 0.12 | 0.45 | 6% |
| | t* | 4459 | - | - | 3 | 0.1 | 0.011 | - | 3 | 0.1 | 0.010 | 10% |
| *S*-wave | 1 Hz | 612 | 30 | 0.79 | 30 | 0.1 | 0.56 | 110% | 30 | 0.1 | 0.51 | 16% |
| | 1 Hz [3] | 629 | 30 | 0.96 | 30 | 0.1 | 0.66 | 120% | 30 | 0.1 | 0.61 | 16% |
| | 2 Hz | 633 | 80 | 0.67 | 30 | 0.1 | 0.46 | 110% | 30 | 0.1 | 0.44 | 13% |
| | 4 Hz | 629 | 160 | 0.64 | 30 | 0.1 | 0.44 | 120% | 30 | 0.1 | 0.43 | 9% |
| | 8 Hz | 348 | 290 | 0.65 | 30 | 0.1 | 0.44 | 120% | 30 | 0.1 | 0.43 | 7% |

[1] Misfits are defined as $\sqrt{\chi^2 / N}$, where $\chi^2$ is defined in equation (16) and $N$ is the number of observations.

[2] Variance is defined as $\chi^2 / N$.

[3] A four second window was used for the spectrum estimates for this inversion.

[4] Shots in the Seattle metropolitan area were excluded from this inversion.

Figure 1

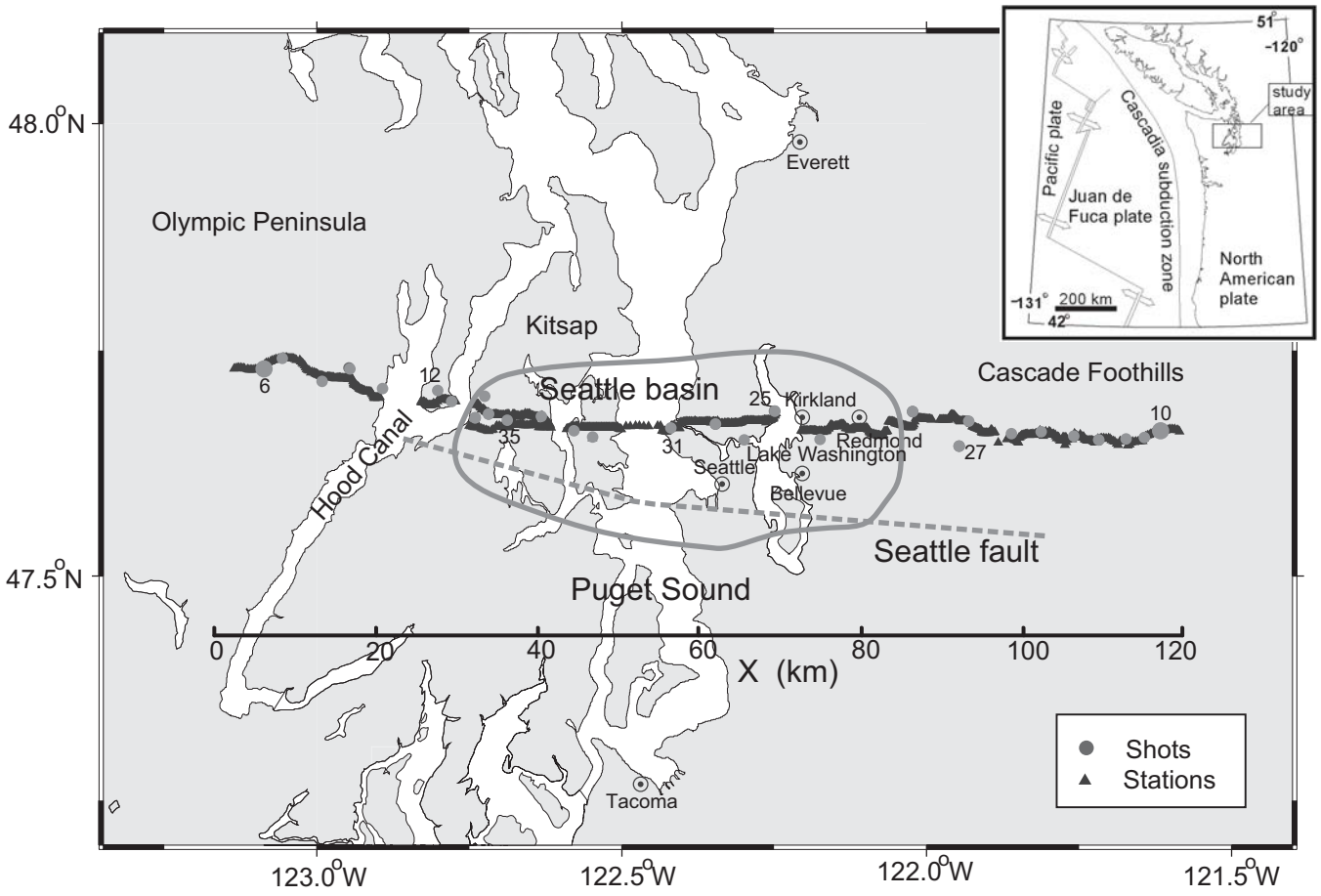
48.0°N
47.5°N
123.0°W
122.5°W
122.0°W
121.5°W
Olympic Peninsula
Kitsap
Everett
Seattle basin
Cascade Foothills
Hood Canal
Kirkland
Redmond
Lake Washington
Seattle
Bellevue
Seattle fault
Puget Sound
Tacoma
6
12
35
31
25
27
10
0
20
40
60
80
100
120
X (km)
Shots
Stations
51°
-120°
study area
Pacific plate
Juan de Fuca plate
Cascadia subduction zone
North American plate
-131°
200 km
42°

Figure 2

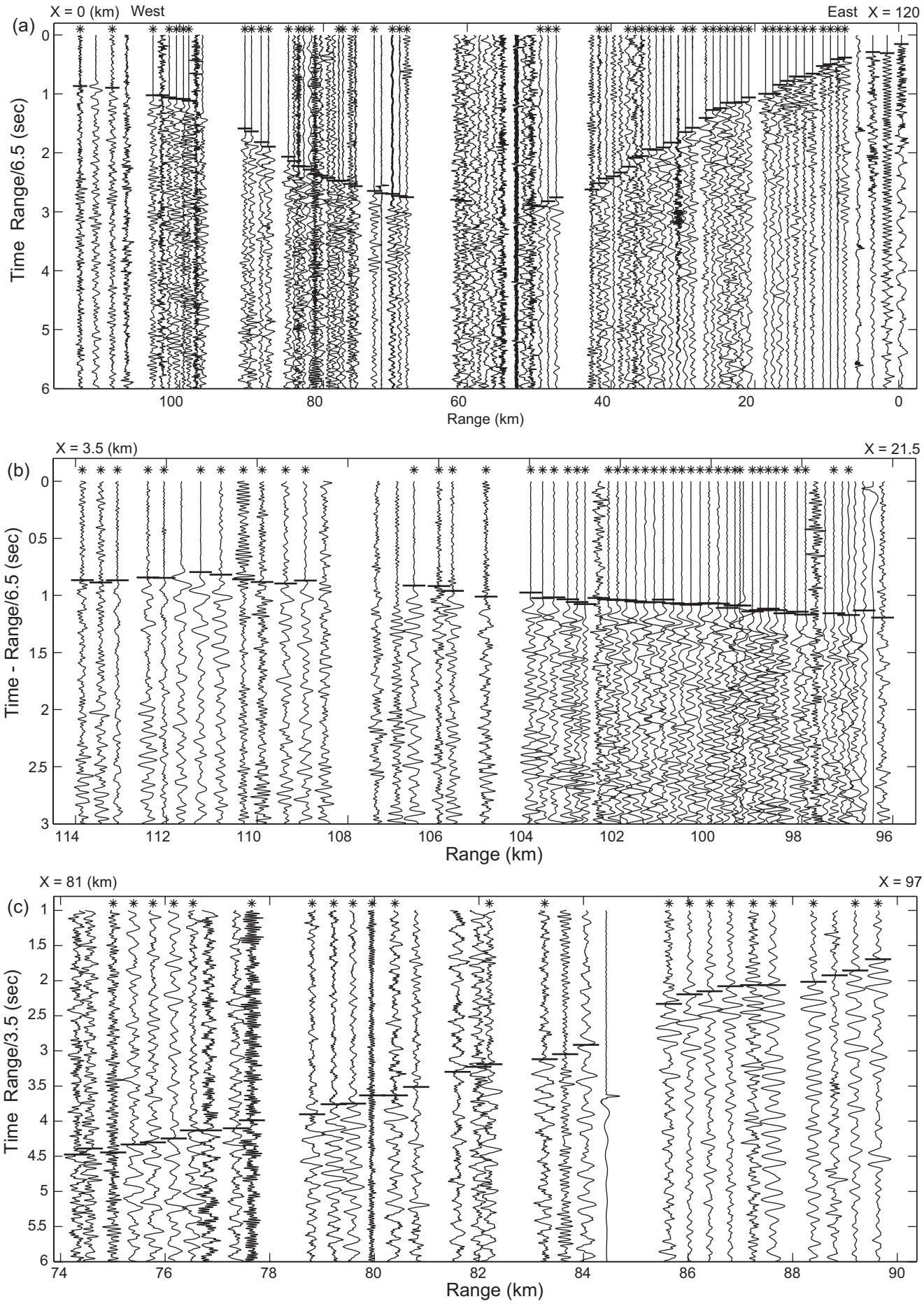
(a)
X = 0 (km) West
East X = 120
Time Range/6.5 (sec)
Range (km)
(b)
X = 3.5 (km)
X = 21.5
Time - Range/6.5 (sec)
Range (km)
(c)
X = 81 (km)
X = 97
Time Range/3.5 (sec)
Range (km)

Figure 3

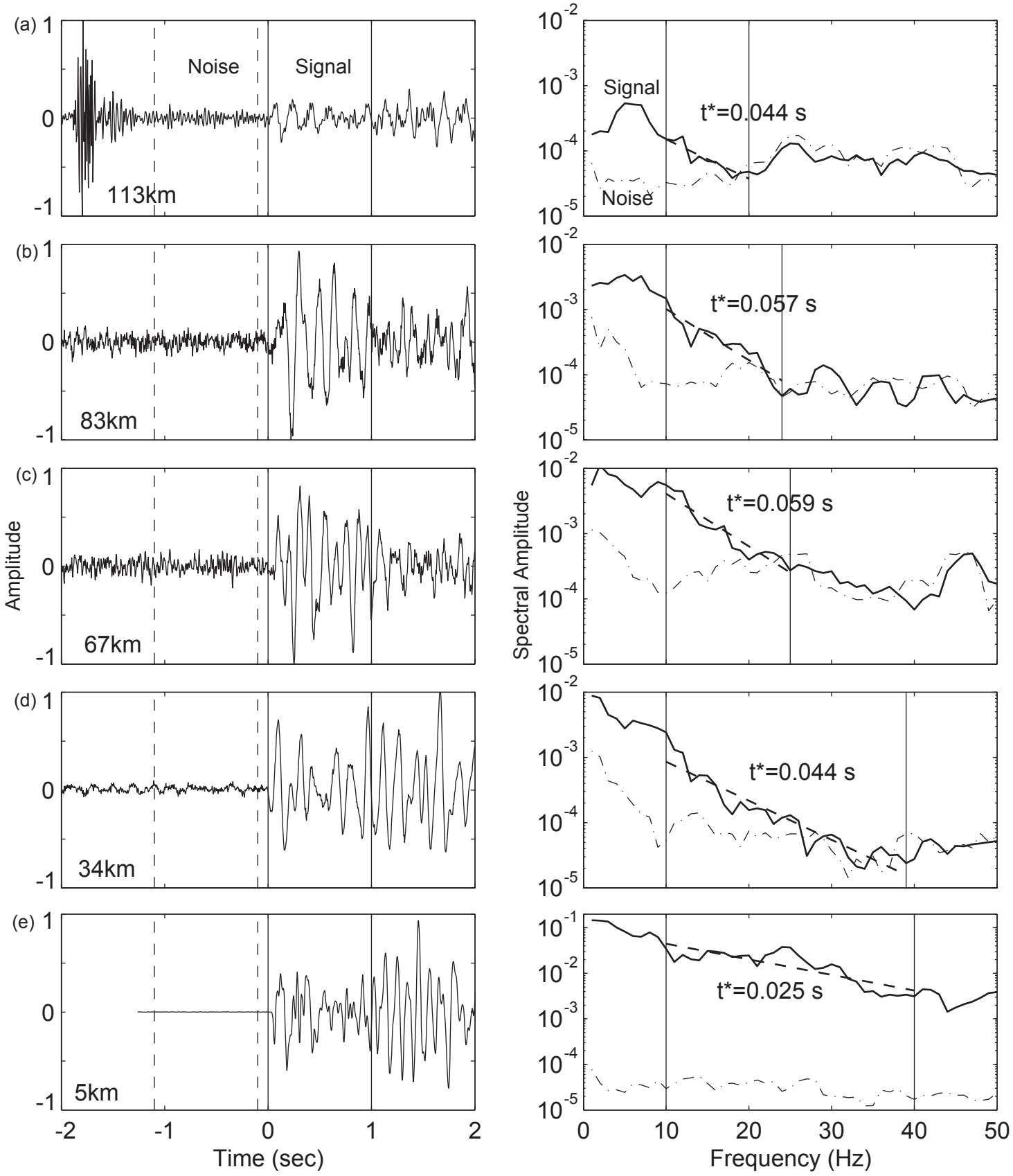
(a)
Noise
Signal
113km
Signal
Noise
t*=0.044 s
(b)
83km
t*=0.057 s
(c)
67km
t*=0.059 s
(d)
34km
t*=0.044 s
(e)
5km
t*=0.025 s
Amplitude
Spectral Amplitude
Time (sec)
Frequency (Hz)

Figure 4

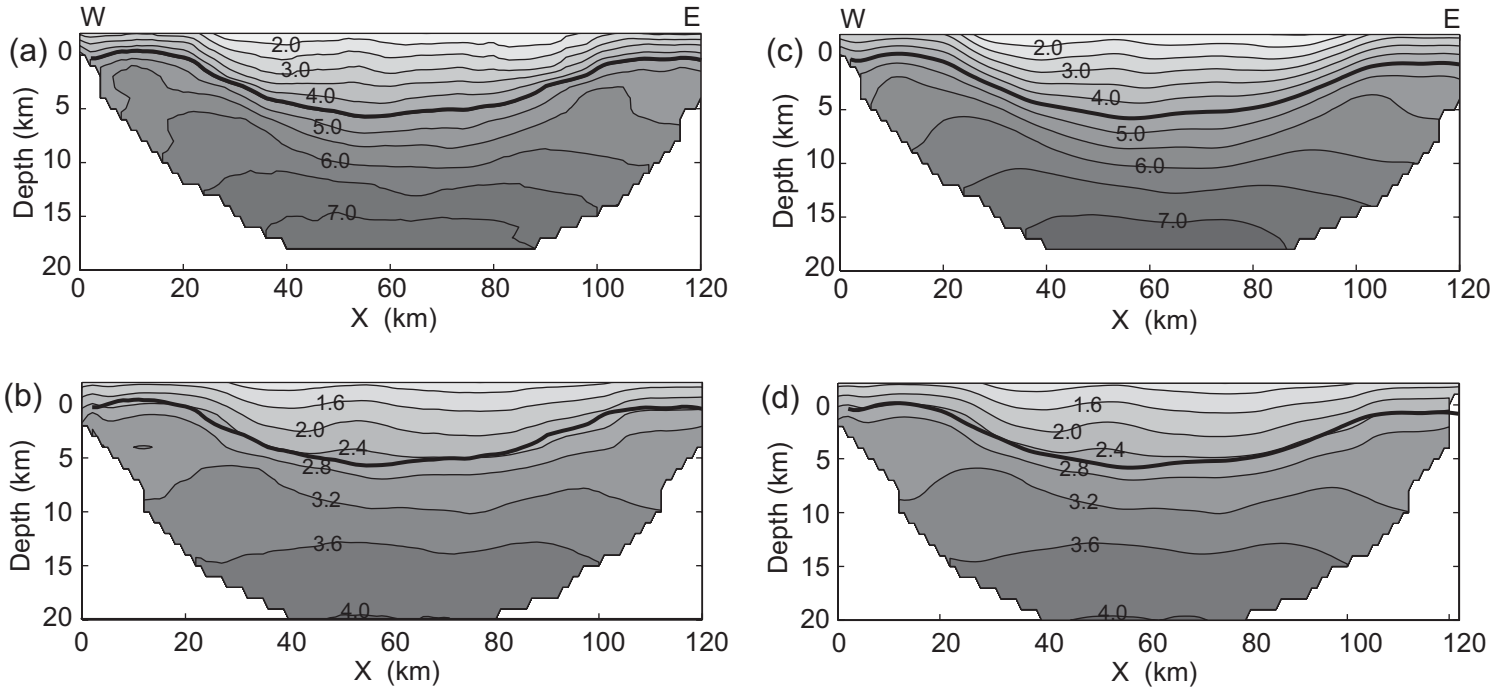

Figure 5

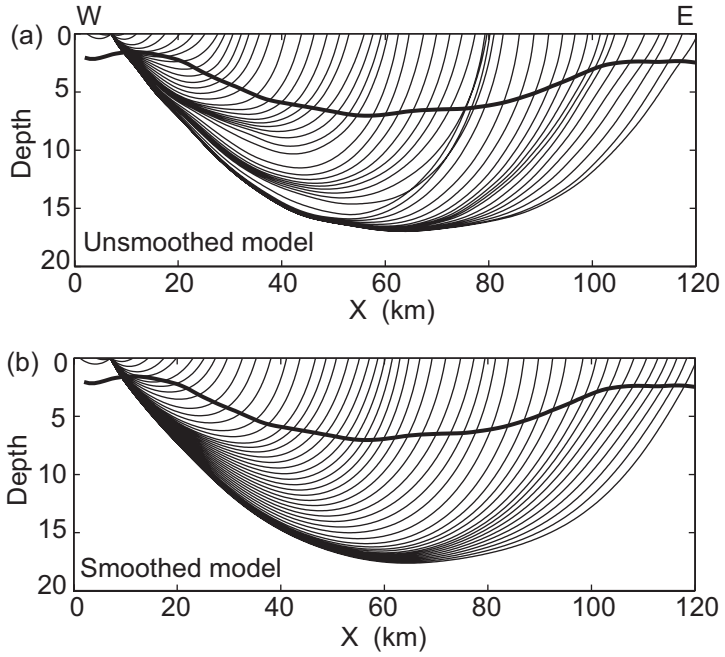
W
E
(a)
Depth
0
5
10
15
20
Unsmoothed model
0
20
40
60
80
100
120
X (km)
(b)
Depth
0
5
10
15
20
Smoothed model
0
20
40
60
80
100
120
X (km)

Figure 6

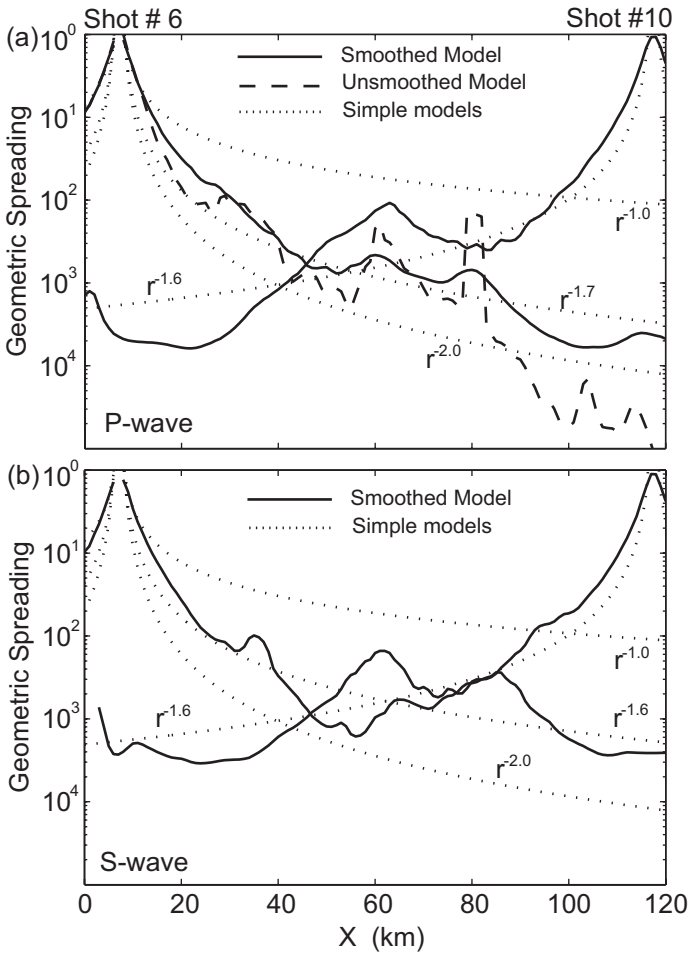
Shot # 6
Shot #10
(a)
Smoothed Model
Unsmoothed Model
Simple models
Geometric Spreading
r-1.0
r-1.6
r-1.7
r-2.0
P-wave
(b)
Smoothed Model
Simple models
Geometric Spreading
r-1.0
r-1.6
r-1.6
r-2.0
S-wave
0
20
40
60
80
100
120
X (km)

Figure 7

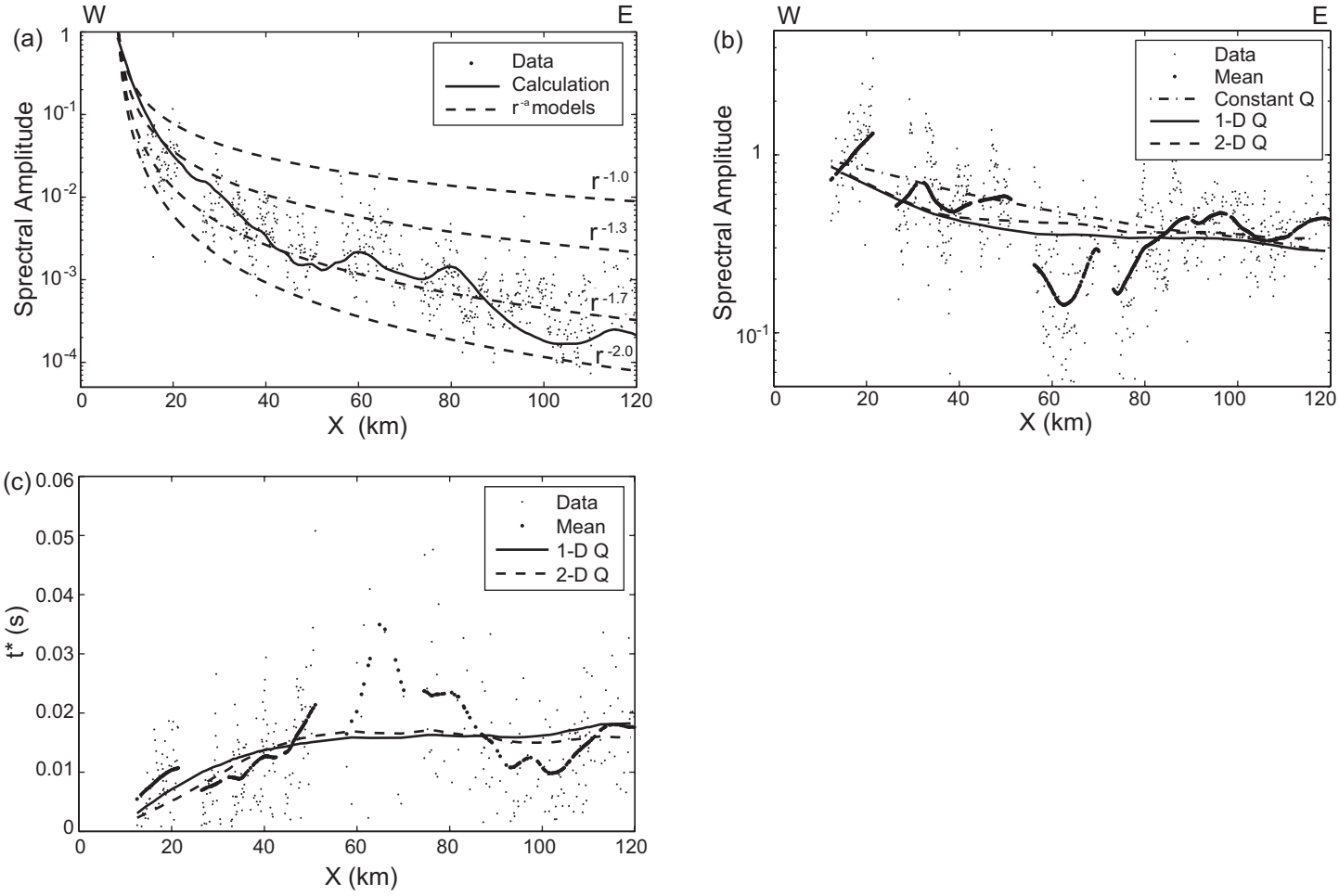
W
E
(a)
Data
Calculation
r^-a models
r^-1.0
r^-1.3
r^-1.7
r^-2.0
Sprectral Amplitude
X (km)
(b)
Data
Mean
Constant Q
1-D Q
2-D Q
Spectral Amplitude
X (km)
(c)
Data
Mean
1-D Q
2-D Q
t* (s)
X (km)

Figure 8

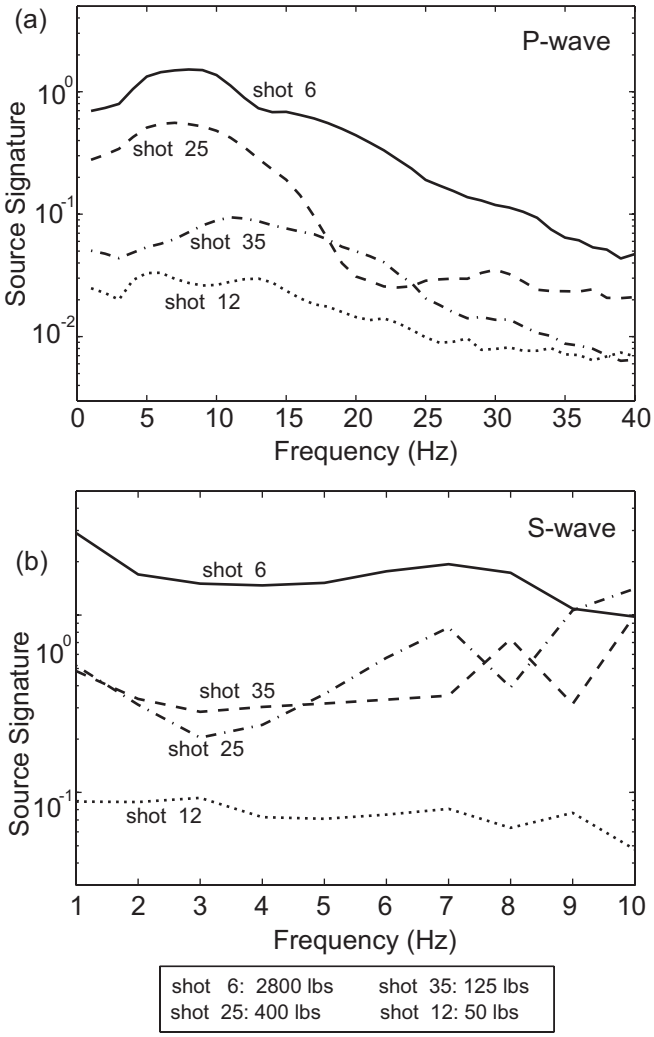
(a)
P-wave
shot 6
shot 25
shot 35
shot 12
Source Signature
$10^0$
$10^{-1}$
$10^{-2}$
0 5 10 15 20 25 30 35 40
Frequency (Hz)
(b)
S-wave
shot 6
shot 35
shot 25
shot 12
Source Signature
$10^0$
$10^{-1}$
1 2 3 4 5 6 7 8 9 10
Frequency (Hz)
shot 6: 2800 lbs
shot 25: 400 lbs
shot 35: 125 lbs
shot 12: 50 lbs

Figure 9

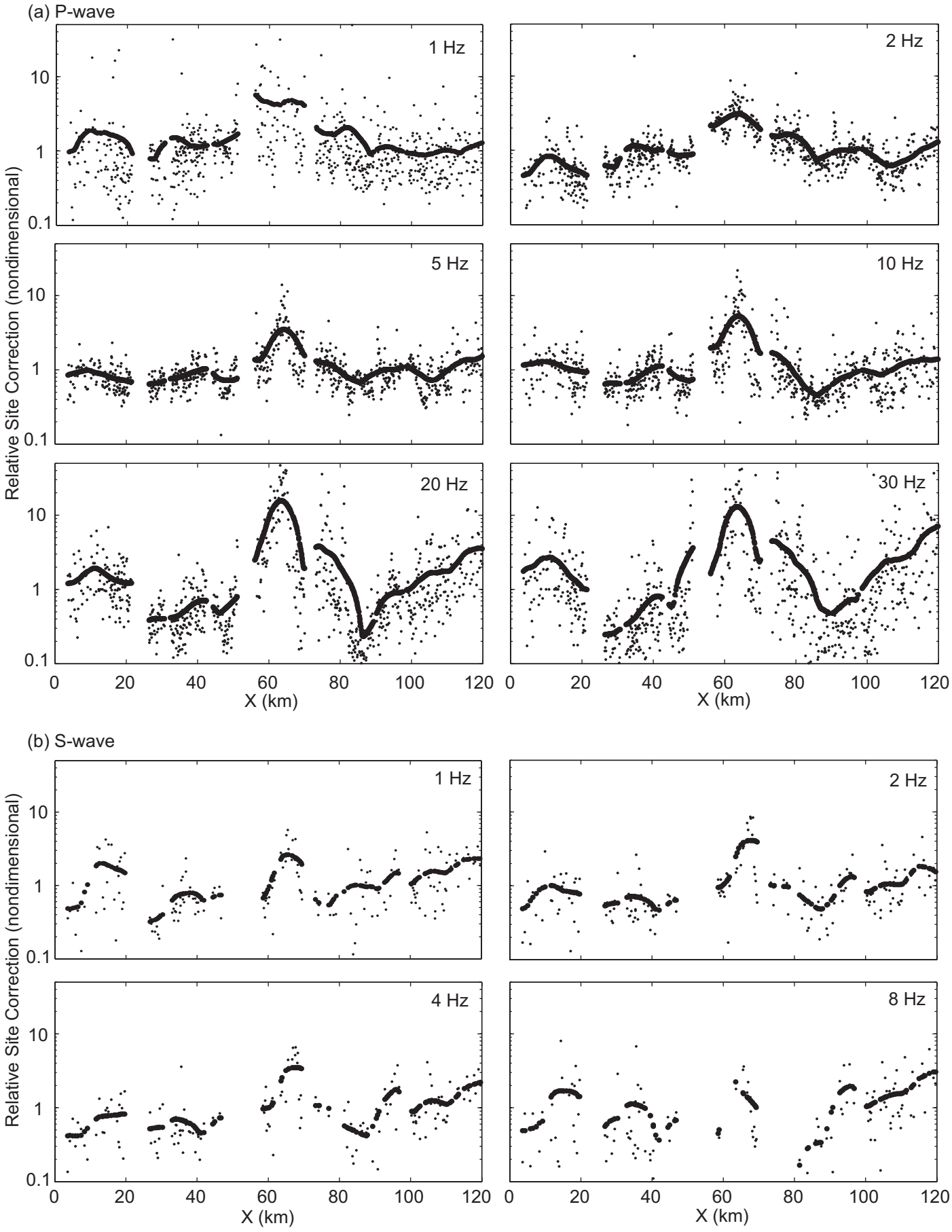
(a) P-wave
1 Hz
2 Hz
5 Hz
10 Hz
20 Hz
30 Hz
Relative Site Correction (nondimensional)
X (km)
(b) S-wave
1 Hz
2 Hz
4 Hz
8 Hz
Relative Site Correction (nondimensional)
X (km)

Figure 10

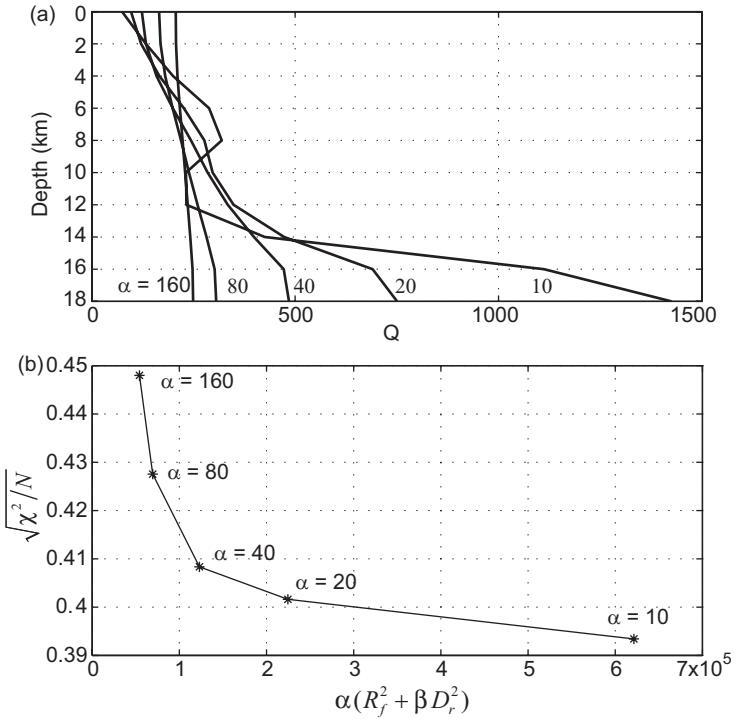
(a)
Depth (km)
Q
α = 160
80
40
20
10
(b)
$\sqrt{\chi^2/N}$
α = 160
α = 80
α = 40
α = 20
α = 10
7x10^5
$\alpha(R_f^2 + \beta D_r^2)$

Figure 11

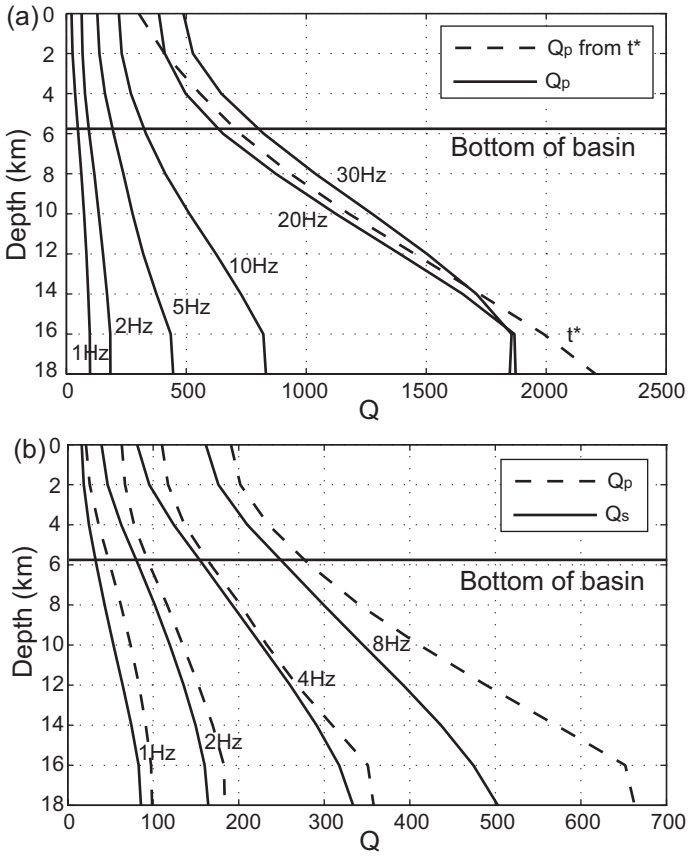
(a)
Depth (km)
Q
Qp from t*
Qp
Bottom of basin
30Hz
20Hz
10Hz
5Hz
2Hz
1Hz
t*
(b)
Depth (km)
Q
Qp
Qs
Bottom of basin
8Hz
4Hz
2Hz
1Hz

Figure 12

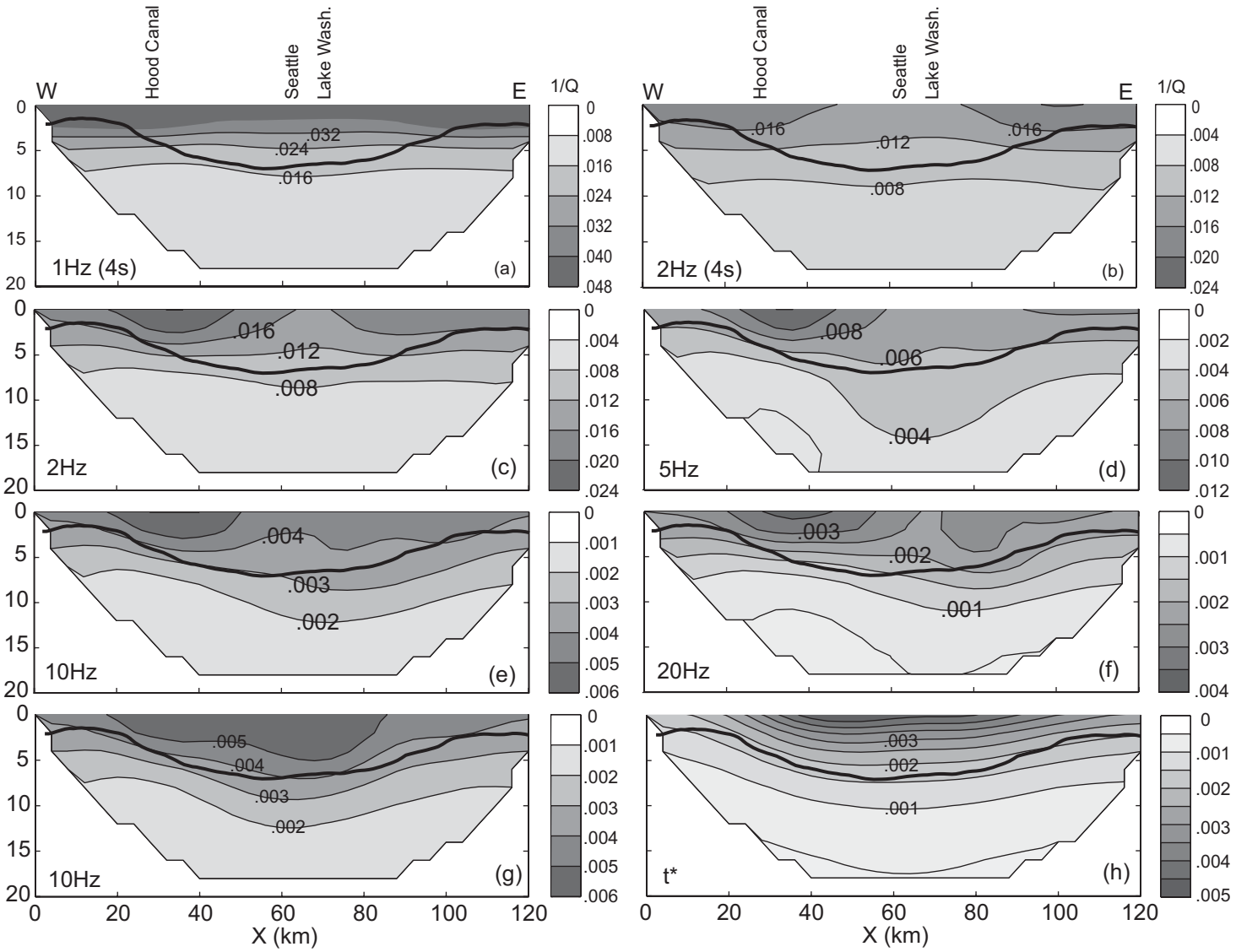
W
Hood Canal
Seattle
Lake Wash.
E
1/Q
1Hz (4s)
(a)
2Hz (4s)
(b)
2Hz
(c)
5Hz
(d)
10Hz
(e)
20Hz
(f)
10Hz
(g)
t*
(h)
X (km)

Figure 13

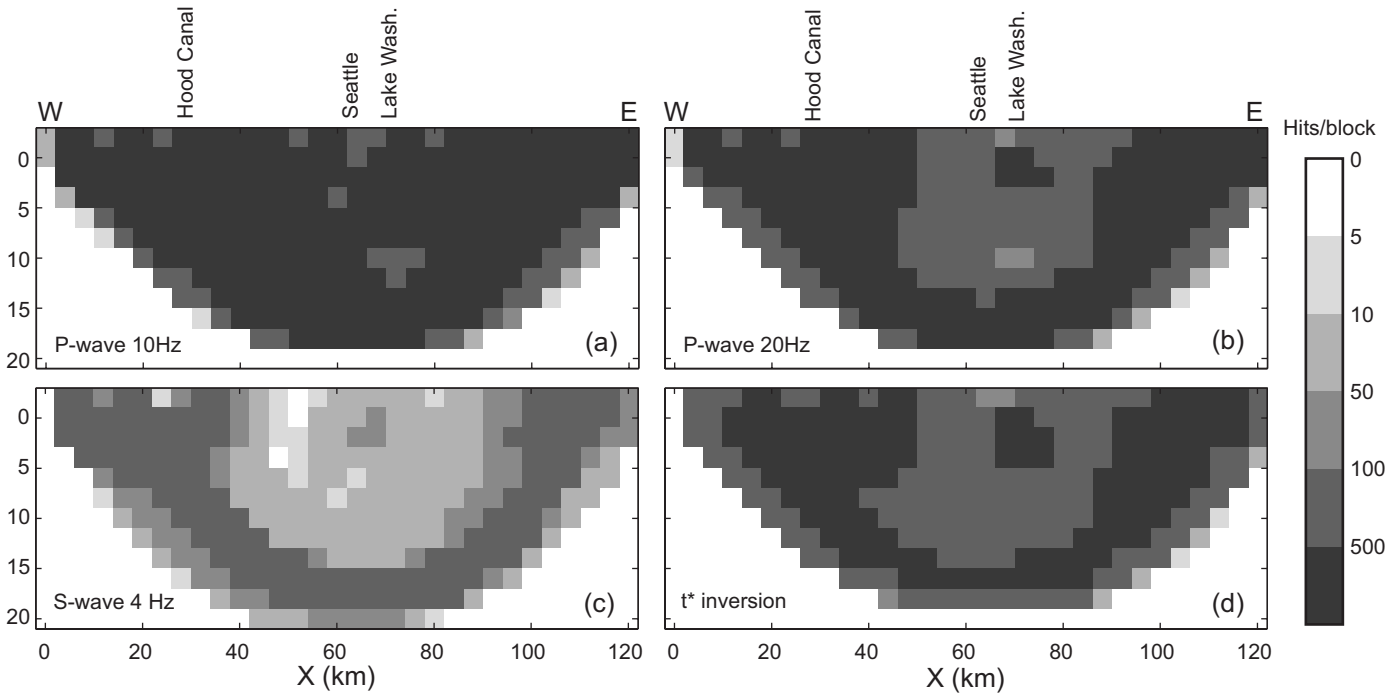
W
Hood Canal
Seattle
Lake Wash.
E
P-wave 10Hz
(a)
P-wave 20Hz
(b)
S-wave 4 Hz
(c)
t* inversion
(d)
0
5
10
15
20
0
20
40
60
80
100
120
X (km)
Hits/block
0
5
10
50
100
500

Figure 14

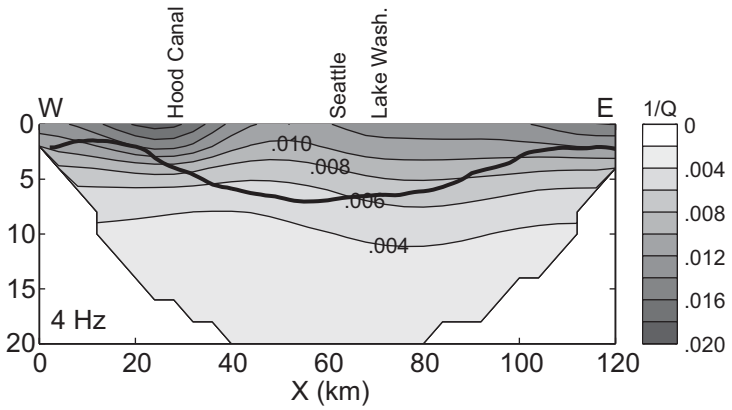
Hood Canal
Seattle
Lake Wash.
W
E
1/Q
0
.004
.008
.012
.016
.020
.010
.008
.006
.004
4 Hz
0
5
10
15
20
0
20
40
60
80
100
120
X (km)

Figure 15

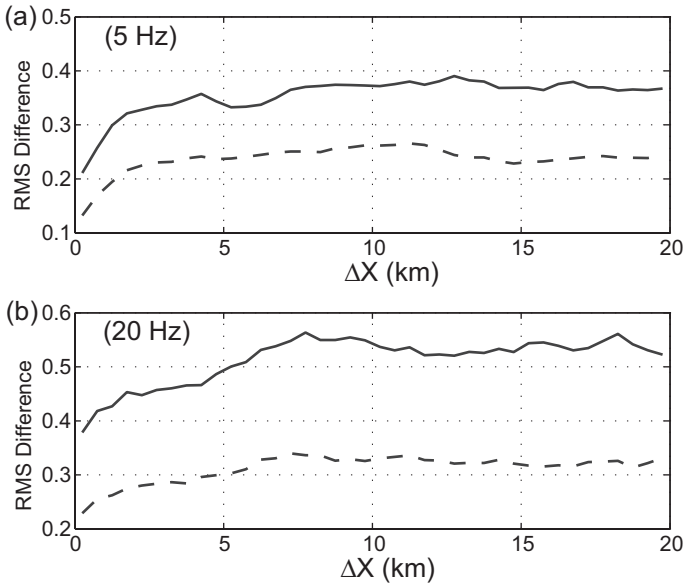
(a)
(5 Hz)
RMS Difference
0.5
0.4
0.3
0.2
0.1
0
5
10
15
20
ΔX (km)
(b)
(20 Hz)
RMS Difference
0.6
0.5
0.4
0.3
0.2
0
5
10
15
20
ΔX (km)

Figure 16

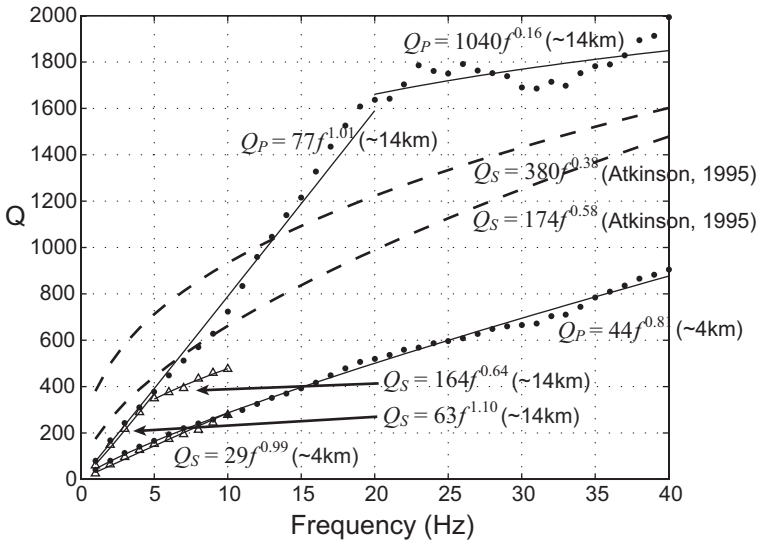
$Q_P = 1040f^{0.16}$ (~14km)
$Q_P = 77f^{1.01}$ (~14km)
$Q_S = 380f^{0.38}$ (Atkinson, 1995)
$Q_S = 174f^{0.58}$ (Atkinson, 1995)
$Q_P = 44f^{0.8}$ (~4km)
$Q_S = 164f^{0.64}$ (~14km)
$Q_S = 63f^{1.10}$ (~14km)
$Q_S = 29f^{0.99}$ (~4km)
Q
Frequency (Hz)
0
200
400
600
800
1000
1200
1400
1600
1800
2000
0
5
10
15
20
25
30
35
40

Figure 17

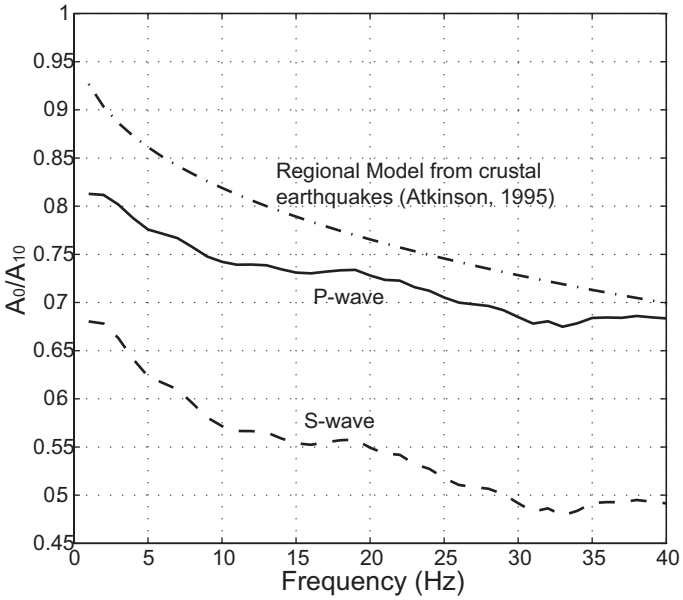
1
0.95
09
0.85
08
0.75
07
0.65
06
0.55
05
0.45
0
5
10
15
20
25
30
35
40
A0/A10
Frequency (Hz)
Regional Model from crustal
earthquakes (Atkinson, 1995)
P-wave
S-wave